

**Fermi National Accelerator Laboratory**

**FERMILAB-Conf-95/177-E**

**DØ**

## **The DØ Upgrade**

**S. Abachi et al.**  
**The DØ Collaboration**  
*Fermi National Accelerator Laboratory*  
*P.O. Box 500, Batavia, Illinois 60510*

**July 1995**

**Submitted to the *International Europhysics Conference on High Energy Physics (HEP 95)*, Brussels, Belgium,  
July 27- August 2, 1995.**

## **Disclaimer**

*This report was prepared as an account of work sponsored by an agency of the United States Government. Neither the United States Government nor any agency thereof, nor any of their employees, makes any warranty, express or implied, or assumes any legal liability or responsibility for the accuracy, completeness, or usefulness of any information, apparatus, product, or process disclosed, or represents that its use would not infringe privately owned rights. Reference herein to any specific commercial product, process, or service by trade name, trademark, manufacturer, or otherwise, does not necessarily constitute or imply its endorsement, recommendation, or favoring by the United States Government or any agency thereof. The views and opinions of authors expressed herein do not necessarily state or reflect those of the United States Government or any agency thereof.*

## The DØ Upgrade

THE DØ COLLABORATION

### ABSTRACT

In this paper we describe the approved DØ Upgrade detector, and its physics capabilities. The DØ Upgrade is under construction and will run during the next Fermilab collider running period in early 1999 (Run II). The upgrade is designed to work at the higher luminosities and shorter bunch spacings expected during this run. The major elements of the upgrade are: a new tracking system with a silicon tracker, scintillating fiber tracker, a 2T solenoid, and a central preshower detector; new calorimeter electronics; new muon trigger and tracking detectors with new muon system electronics; a forward preshower detector; new trigger electronics and DAQ improvements to handle the higher rates.

Submitted to the International Europhysics Conference on High  
Energy Physics (HEP 95), Brussels, Belgium, 27 July - 2 August 1995.

S. Abachi,<sup>12</sup> B. Abbott,<sup>34</sup> M. Abolins,<sup>23</sup> B.S. Acharya,<sup>41</sup> I. Adam,<sup>10</sup> D.L. Adams,<sup>35</sup> M. Adams,<sup>15</sup>  
 S. Ahn,<sup>12</sup> H. Aihara,<sup>20</sup> J. Alitti,<sup>37</sup> G. Álvarez,<sup>16</sup> G.A. Alves,<sup>8</sup> E. Amidi,<sup>27</sup> N. Amos,<sup>22</sup> E.W. Anderson,<sup>17</sup>  
 S.H. Aronson,<sup>3</sup> R. Astur,<sup>39</sup> R.E. Avery,<sup>29</sup> A. Baden,<sup>21</sup> V. Balamurali,<sup>30</sup> J. Balderston,<sup>14</sup> B. Baldin,<sup>12</sup>  
 J. Bantly,<sup>4</sup> J.F. Bartlett,<sup>12</sup> K. Bazizi,<sup>7</sup> J. Bendich,<sup>20</sup> S.B. Beri,<sup>32</sup> I. Bertram,<sup>35</sup> V.A. Bezzubov,<sup>33</sup> P.C. Bhat,<sup>12</sup>  
 V. Bhatnagar,<sup>32</sup> M. Bhattacharjee,<sup>11</sup> A. Bischoff,<sup>7</sup> N. Biswas,<sup>30</sup> G. Blazey,<sup>12</sup> S. Blessing,<sup>13</sup> P. Bloom,<sup>5</sup>  
 A. Boehnlein,<sup>12</sup> N.I. Bojko,<sup>33</sup> F. Borchering,<sup>12</sup> J. Borders,<sup>36</sup> C. Boswell,<sup>7</sup> A. Brandt,<sup>12</sup> R. Brock,<sup>23</sup>  
 A. Bross,<sup>12</sup> D. Buchholz,<sup>29</sup> V.S. Burtovoi,<sup>33</sup> J.M. Butler,<sup>12</sup> D. Casey,<sup>36</sup> H. Castilla-Valdez,<sup>9</sup> D. Chakraborty,<sup>39</sup>  
 S.-M. Chang,<sup>27</sup> S.V. Chekulaev,<sup>33</sup> L.-P. Chen,<sup>20</sup> W. Chen,<sup>39</sup> L. Chevalier,<sup>37</sup> S. Chopra,<sup>32</sup> B.C. Choudhary,<sup>7</sup>  
 J.H. Christenson,<sup>12</sup> M. Chung,<sup>15</sup> D. Claes,<sup>39</sup> A.R. Clark,<sup>20</sup> W.G. Cobau,<sup>21</sup> J. Cochran,<sup>7</sup> W.E. Cooper,<sup>12</sup>  
 C. Cretsinger,<sup>36</sup> D. Cullen-Vidal,<sup>4</sup> M.A.C. Cummings,<sup>14</sup> D. Cutts,<sup>4</sup> O.I. Dahl,<sup>20</sup> K. De,<sup>42</sup> M. Demarteau,<sup>12</sup>  
 R. Demina,<sup>27</sup> K. Denisenko,<sup>12</sup> N. Denisenko,<sup>12</sup> D. Denisov,<sup>12</sup> S.P. Denisov,<sup>33</sup> W. Dharmaratna,<sup>13</sup>  
 H.T. Diehl,<sup>12</sup> M. Diesburg,<sup>12</sup> G. Di Loreto,<sup>23</sup> R. Dixon,<sup>12</sup> P. Draper,<sup>42</sup> J. Drinkard,<sup>6</sup> Y. Ducros,<sup>37</sup>  
 S.R. Dugad,<sup>41</sup> S. Durston-Johnson,<sup>36</sup> D. Edmunds,<sup>23</sup> J. Ellison,<sup>7</sup> V.D. Elvira,<sup>12,†</sup> R. Engelmann,<sup>39</sup>  
 S. Eno,<sup>21</sup> G. Eppley,<sup>35</sup> P. Ermolov,<sup>24</sup> O.V. Eroshin,<sup>33</sup> V.N. Evdokimov,<sup>33</sup> S. Fahey,<sup>23</sup> T. Fahland,<sup>4</sup>  
 M. Fatyga,<sup>3</sup> M.K. Fatyga,<sup>36</sup> J. Featherly,<sup>3</sup> S. Feher,<sup>39</sup> D. Fein,<sup>2</sup> T. Ferbel,<sup>36</sup> G. Finocchiaro,<sup>39</sup> H.E. Fisk,<sup>12</sup>  
 Yu. Fisyak,<sup>24</sup> E. Flattum,<sup>23</sup> G.E. Forden,<sup>2</sup> M. Fortner,<sup>28</sup> K.C. Frame,<sup>23</sup> P. Franzini,<sup>10</sup> S. Fuess,<sup>12</sup>  
 A.N. Galjaev,<sup>33</sup> E. Gallas,<sup>42</sup> C.S. Gao,<sup>12,\*</sup> S. Gao,<sup>12,\*</sup> T.L. Geld,<sup>23</sup> R.J. Genik II,<sup>23</sup> K. Genser,<sup>12</sup>  
 C.E. Gerber,<sup>12,§</sup> B. Gibbard,<sup>3</sup> V. Glebov,<sup>36</sup> S. Glenn,<sup>5</sup> B. Gobbi,<sup>29</sup> M. Goforth,<sup>13</sup> A. Goldschmidt,<sup>20</sup>  
 B. Gómez,<sup>1</sup> P.I. Goncharov,<sup>33</sup> H. Gordon,<sup>3</sup> L.T. Goss,<sup>43</sup> N. Graf,<sup>3</sup> P.D. Grannis,<sup>39</sup> D.R. Green,<sup>12</sup> J. Green,<sup>28</sup>  
 H. Greenlee,<sup>12</sup> G. Griffin,<sup>6</sup> N. Grossman,<sup>12</sup> P. Grudberg,<sup>20</sup> S. Grünendahl,<sup>36</sup> W. Gu,<sup>12,\*</sup> G. Guglielmo,<sup>31</sup>  
 J.A. Guida,<sup>39</sup> J.M. Guida,<sup>3</sup> W. Guryn,<sup>3</sup> S.N. Gurzhev,<sup>33</sup> P. Gutierrez,<sup>31</sup> Y.E. Gutnikov,<sup>33</sup> N.J. Hadley,<sup>21</sup>  
 H. Haggerty,<sup>12</sup> S. Hagopian,<sup>13</sup> V. Hagopian,<sup>13</sup> K.S. Hahn,<sup>36</sup> R.E. Hall,<sup>6</sup> S. Hansen,<sup>12</sup> R. Hatcher,<sup>23</sup>  
 J.M. Hauptman,<sup>17</sup> D. Hedin,<sup>28</sup> A.P. Heinson,<sup>7</sup> U. Heintz,<sup>12</sup> R. Hernández-Montoya,<sup>9</sup> T. Heuring,<sup>13</sup>  
 R. Hirosky,<sup>13</sup> J.D. Hobbs,<sup>12</sup> B. Hoeneisen,<sup>1,¶</sup> J.S. Hoftun,<sup>4</sup> F. Hsieh,<sup>22</sup> Ting Hu,<sup>39</sup> Tong Hu,<sup>16</sup> T. Huehn,<sup>7</sup>  
 S. Igarashi,<sup>12</sup> A.S. Ito,<sup>12</sup> E. James,<sup>2</sup> J. Jaques,<sup>30</sup> S.A. Jerger,<sup>23</sup> J.Z.-Y. Jiang,<sup>39</sup> T. Joffe-Minor,<sup>29</sup>  
 H. Johari,<sup>27</sup> K. Johns,<sup>2</sup> M. Johnson,<sup>12</sup> H. Johnstad,<sup>40</sup> A. Jonckheere,<sup>12</sup> M. Jones,<sup>14</sup> H. Jöstlein,<sup>12</sup> S.Y. Jun,<sup>29</sup>  
 C.K. Jung,<sup>39</sup> S. Kahn,<sup>3</sup> G. Kalbfleisch,<sup>31</sup> J.S. Kang,<sup>18</sup> R. Kehoe,<sup>30</sup> M.L. Kelly,<sup>30</sup> A. Kernan,<sup>7</sup> L. Kerth,<sup>20</sup>  
 C.L. Kim,<sup>18</sup> S.K. Kim,<sup>38</sup> A. Klatchko,<sup>13</sup> B. Klima,<sup>12</sup> B.I. Klochkov,<sup>33</sup> C. Klopfenstein,<sup>39</sup> V.I. Klyukhin,<sup>33</sup>  
 V.I. Kochetkov,<sup>33</sup> J.M. Kohli,<sup>32</sup> D. Koltick,<sup>34</sup> A.V. Kostritskiy,<sup>33</sup> J. Kotcher,<sup>3</sup> J. Kourlas,<sup>26</sup> A.V. Kozelov,<sup>33</sup>  
 E.A. Kozlovski,<sup>33</sup> M.R. Krishnaswamy,<sup>41</sup> S. Krzywdzinski,<sup>12</sup> S. Kunori,<sup>21</sup> S. Lami,<sup>39</sup> G. Landsberg,<sup>12</sup>  
 R.E. Lanou,<sup>4</sup> J-F. Lebrat,<sup>37</sup> A. Leflat,<sup>24</sup> H. Li,<sup>39</sup> J. Li,<sup>42</sup> Y.K. Li,<sup>29</sup> Q.Z. Li-Demarteau,<sup>12</sup> J.G.R. Lima,<sup>8</sup>  
 D. Lincoln,<sup>22</sup> S.L. Linn,<sup>13</sup> J. Linnemann,<sup>23</sup> R. Lipton,<sup>12</sup> Y.C. Liu,<sup>29</sup> F. Lobkowicz,<sup>36</sup> S.C. Loken,<sup>20</sup>  
 S. Lökös,<sup>39</sup> L. Lueking,<sup>12</sup> A.L. Lyon,<sup>21</sup> A.K.A. Maciel,<sup>8</sup> R.J. Madaras,<sup>20</sup> R. Madden,<sup>13</sup> I.V. Mandrichenko,<sup>33</sup>  
 Ph. Mangeot,<sup>37</sup> S. Mani,<sup>5</sup> B. Mansoulié,<sup>37</sup> H.S. Mao,<sup>12,\*</sup> S. Margulies,<sup>15</sup> R. Markeloff,<sup>28</sup> L. Markosky,<sup>2</sup>  
 T. Marshall,<sup>16</sup> M.I. Martin,<sup>12</sup> M. Marx,<sup>39</sup> B. May,<sup>29</sup> A.A. Mayorov,<sup>33</sup> R. McCarthy,<sup>39</sup> T. McKibben,<sup>15</sup>  
 J. McKinley,<sup>23</sup> T. McMahon,<sup>31</sup> H.L. Melanson,<sup>12</sup> J.R.T. de Mello Neto,<sup>8</sup> K.W. Merritt,<sup>12</sup> H. Miettinen,<sup>35</sup>  
 A. Milder,<sup>2</sup> A. Mincer,<sup>26</sup> J.M. de Miranda,<sup>8</sup> C.S. Mishra,<sup>12</sup> M. Mohammadi-Baarmand,<sup>39</sup> N. Mokhov,<sup>12</sup>  
 N.K. Mondal,<sup>41</sup> H.E. Montgomery,<sup>12</sup> P. Mooney,<sup>1</sup> M. Mudan,<sup>26</sup> C. Murphy,<sup>16</sup> C.T. Murphy,<sup>12</sup> F. Nang,<sup>4</sup>  
 M. Narain,<sup>12</sup> V.S. Narasimham,<sup>41</sup> A. Narayanan,<sup>2</sup> H.A. Neal,<sup>22</sup> J.P. Negret,<sup>1</sup> E. Neis,<sup>22</sup> P. Nemethy,<sup>26</sup>  
 D. Nešić,<sup>4</sup> D. Norman,<sup>43</sup> L. Oesch,<sup>22</sup> V. Oguri,<sup>8</sup> E. Oltman,<sup>20</sup> N. Oshima,<sup>12</sup> D. Owen,<sup>23</sup> P. Padley,<sup>35</sup>  
 M. Pang,<sup>17</sup> A. Para,<sup>12</sup> C.H. Park,<sup>12</sup> Y.M. Park,<sup>19</sup> R. Partridge,<sup>4</sup> N. Parua,<sup>41</sup> M. Paterno,<sup>36</sup> J. Perkins,<sup>42</sup>  
 A. Peryshkin,<sup>12</sup> M. Peters,<sup>14</sup> H. Piekarczyk,<sup>13</sup> Y. Pischalnikov,<sup>34</sup> A. Pluquet,<sup>37</sup> V.M. Podstavkov,<sup>33</sup> B.G. Pope,<sup>23</sup>  
 H.B. Prosper,<sup>13</sup> S. Protopopescu,<sup>3</sup> D. Pušeljčić,<sup>20</sup> J. Qian,<sup>22</sup> P.Z. Quintas,<sup>12</sup> R. Raja,<sup>12</sup> S. Rajagopalan,<sup>39</sup>

O. Ramirez,<sup>15</sup> M.V.S. Rao,<sup>41</sup> P.A. Rapidis,<sup>12</sup> L. Rasmussen,<sup>39</sup> A.L. Read,<sup>12</sup> S. Reucroft,<sup>27</sup> M. Rijssenbeek,<sup>39</sup> T. Rockwell,<sup>23</sup> N.A. Roe,<sup>20</sup> P. Rubinov,<sup>39</sup> R. Ruchti,<sup>30</sup> S. Rusin,<sup>24</sup> J. Rutherford,<sup>2</sup> A. Santoro,<sup>8</sup> L. Sawyer,<sup>42</sup> R.D. Schamberger,<sup>39</sup> H. Schellman,<sup>29</sup> J. Sculli,<sup>26</sup> E. Shabalina,<sup>24</sup> C. Shaffer,<sup>13</sup> H.C. Shankar,<sup>41</sup> R.K. Shivpuri,<sup>11</sup> M. Shupe,<sup>2</sup> J.B. Singh,<sup>32</sup> V. Sirotenko,<sup>28</sup> W. Smart,<sup>12</sup> A. Smith,<sup>2</sup> R.P. Smith,<sup>12</sup> R. Snihur,<sup>29</sup> G.R. Snow,<sup>25</sup> S. Snyder,<sup>39</sup> J. Solomon,<sup>15</sup> P.M. Sood,<sup>32</sup> M. Sosebee,<sup>42</sup> M. Souza,<sup>8</sup> A.L. Spadafora,<sup>20</sup> R.W. Stephens,<sup>42</sup> M.L. Stevenson,<sup>20</sup> D. Stewart,<sup>22</sup> D.A. Stoianova,<sup>33</sup> D. Stoker,<sup>6</sup> K. Streets,<sup>26</sup> M. Strovink,<sup>20</sup> A. Taketani,<sup>12</sup> P. Tamburello,<sup>21</sup> J. Tarazi,<sup>6</sup> M. Tartaglia,<sup>12</sup> T.L. Taylor,<sup>29</sup> J. Teiger,<sup>37</sup> J. Thompson,<sup>21</sup> T.G. Trippe,<sup>20</sup> P.M. Tuts,<sup>10</sup> N. Varelas,<sup>23</sup> E.W. Varnes,<sup>20</sup> P.R.G. Virador,<sup>20</sup> D. Vititoe,<sup>2</sup> A.A. Volkov,<sup>33</sup> A.P. Vorobiev,<sup>33</sup> H.D. Wahl,<sup>13</sup> G. Wang,<sup>13</sup> J. Wang,<sup>12,\*</sup> L.Z. Wang,<sup>12,\*</sup> J. Warchol,<sup>30</sup> M. Wayne,<sup>30</sup> H. Weerts,<sup>23</sup> F. Wen,<sup>13</sup> W.A. Wenzel,<sup>20</sup> A. White,<sup>42</sup> J.T. White,<sup>43</sup> J.A. Wightman,<sup>17</sup> J. Wilcox,<sup>27</sup> S. Willis,<sup>28</sup> S.J. Wimpenny,<sup>7</sup> J.V.D. Wirjawan,<sup>43</sup> J. Womersley,<sup>12</sup> E. Won,<sup>36</sup> D.R. Wood,<sup>12</sup> H. Xu,<sup>4</sup> R. Yamada,<sup>12</sup> P. Yamin,<sup>3</sup> C. Yanagisawa,<sup>39</sup> J. Yang,<sup>26</sup> T. Yasuda,<sup>27</sup> C. Yoshikawa,<sup>14</sup> S. Youssef,<sup>13</sup> J. Yu,<sup>36</sup> Y. Yu,<sup>38</sup> Y. Zhang,<sup>12,\*</sup> Y.H. Zhou,<sup>12,\*</sup> Q. Zhu,<sup>26</sup> Y.S. Zhu,<sup>12,\*</sup> Z.H. Zhu,<sup>36</sup> D. Zieminska,<sup>16</sup> A. Zieminski,<sup>16</sup> and A. Zylberstein<sup>37</sup>

<sup>1</sup>Universidad de los Andes, Bogotá, Colombia

<sup>2</sup>University of Arizona, Tucson, Arizona 85721

<sup>3</sup>Brookhaven National Laboratory, Upton, New York 11973

<sup>4</sup>Brown University, Providence, Rhode Island 02912

<sup>5</sup>University of California, Davis, California 95616

<sup>6</sup>University of California, Irvine, California 92717

<sup>7</sup>University of California, Riverside, California 92521

<sup>8</sup>LAFEX, Centro Brasileiro de Pesquisas Físicas, Rio de Janeiro, Brazil

<sup>9</sup>CINVESTAV, Mexico City, Mexico

<sup>10</sup>Columbia University, New York, New York 10027

<sup>11</sup>Delhi University, Delhi, India 110007

<sup>12</sup>Fermi National Accelerator Laboratory, Batavia, Illinois 60510

<sup>13</sup>Florida State University, Tallahassee, Florida 32306

<sup>14</sup>University of Hawaii, Honolulu, Hawaii 96822

<sup>15</sup>University of Illinois at Chicago, Chicago, Illinois 60607

<sup>16</sup>Indiana University, Bloomington, Indiana 47405

<sup>17</sup>Iowa State University, Ames, Iowa 50011

<sup>18</sup>Korea University, Seoul, Korea

<sup>19</sup>Kyungshung University, Pusan, Korea

<sup>20</sup>Lawrence Berkeley Laboratory and University of California, Berkeley, California 94720

<sup>21</sup>University of Maryland, College Park, Maryland 20742

<sup>22</sup>University of Michigan, Ann Arbor, Michigan 48109

<sup>23</sup>Michigan State University, East Lansing, Michigan 48824

<sup>24</sup>Moscow State University, Moscow, Russia

<sup>25</sup>University of Nebraska, Lincoln, Nebraska 68588

<sup>26</sup>New York University, New York, New York 10003

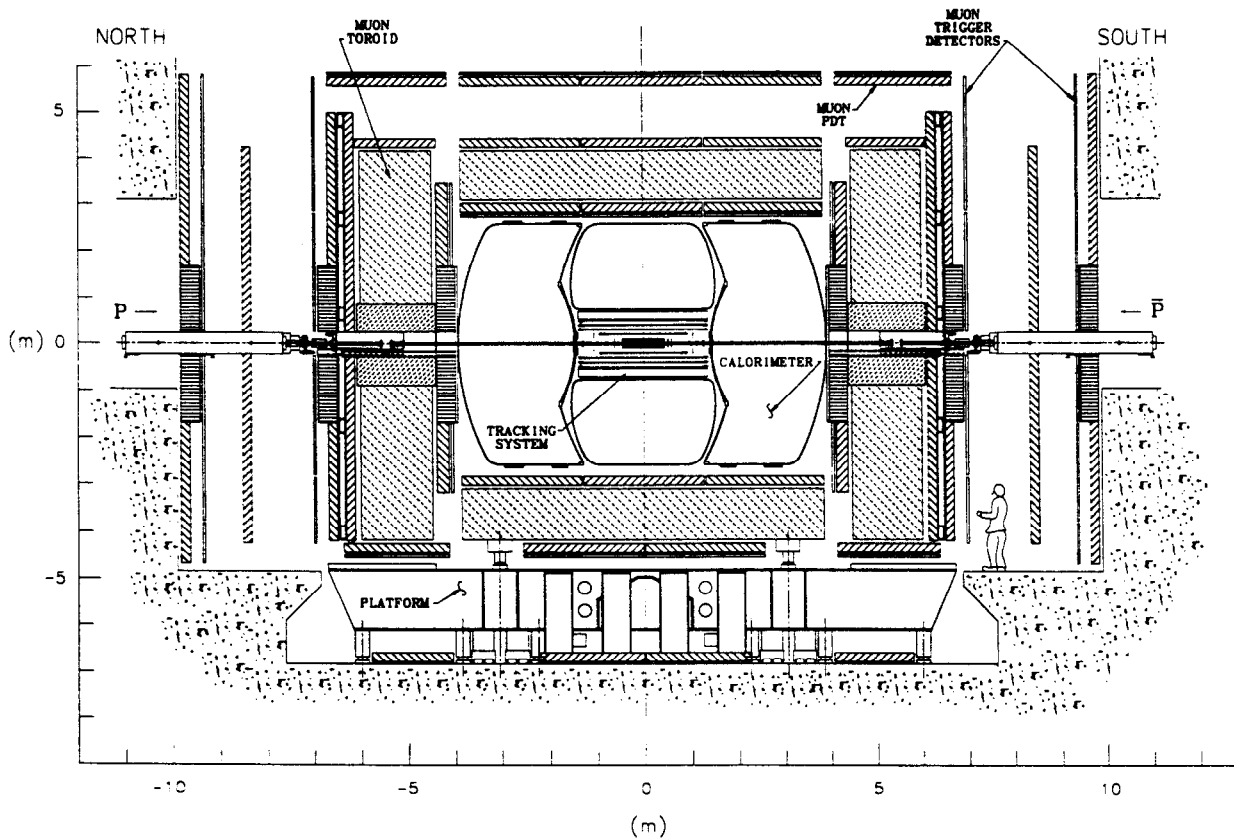
<sup>27</sup>Northeastern University, Boston, Massachusetts 02115

<sup>28</sup>Northern Illinois University, DeKalb, Illinois 60115

- <sup>29</sup>Northwestern University, Evanston, Illinois 60208
- <sup>30</sup>University of Notre Dame, Notre Dame, Indiana 46556
- <sup>31</sup>University of Oklahoma, Norman, Oklahoma 73019
- <sup>32</sup>University of Panjab, Chandigarh 16-00-14, India
- <sup>33</sup>Institute for High Energy Physics, 142-284 Protvino, Russia
- <sup>34</sup>Purdue University, West Lafayette, Indiana 47907
- <sup>35</sup>Rice University, Houston, Texas 77251
- <sup>36</sup>University of Rochester, Rochester, New York 14627
- <sup>37</sup>CEA, DAPNIA/Service de Physique des Particules, CE-SACLAY, France
- <sup>38</sup>Seoul National University, Seoul, Korea
- <sup>39</sup>State University of New York, Stony Brook, New York 11794
- <sup>40</sup>SSC Laboratory, Dallas, Texas 75237
- <sup>41</sup>Tata Institute of Fundamental Research, Colaba, Bombay 400005, India
- <sup>42</sup>University of Texas, Arlington, Texas 76019
- <sup>43</sup>Texas A&M University, College Station, Texas 77843

# 1. Overview of the Upgrade

The  $D\bar{O}$  upgrade will be a key element of the attack on physics in the new high luminosity Main Injector environment. The upgrade plan,<sup>[1]</sup> first proposed in October 1990, has been endorsed by the PAC and Director's Review. It builds on the strengths of  $D\bar{O}$ , full coverage in calorimetry and muon detection, while enhancing the tracking and triggering capabilities. Construction is now underway on a number of the detector systems. It is thus an appropriate juncture at which to review the  $D\bar{O}$  upgrade detector systems and the physics performance we will achieve with the upgrade.



Plotted Mon Apr 17 09:15 '95 CDT 1995 by metaski

Figure 1. The  $D\bar{O}$  upgrade detector.

In Section 2 we summarize the design of the major upgrade detector systems sufficient to give a broad overview, without excess detail. An overall view of the  $D\bar{O}$  detector is shown in Fig. 1 with the primary detector systems indicated. A major element of the upgrade is the replacement of the inner tracking systems, required because of the expected radiation damage to those detectors by Run II and also to improve the physics capabilities of the  $D\bar{O}$  detector. The upgraded tracking system consists of an inner silicon vertex detector, surrounded by four superlayers of scintillating fiber tracker. These detectors are located inside a 2 Tesla superconducting solenoid. A scintillator based central preshower detector with wavelength shifter readout is located between the outer radius of the solenoid and the inner radius of the central calorimeter cryostat to provide electron identification and to compensate for energy losses in the solenoid. A detailed view of the  $D\bar{O}$  upgrade

tracking system is shown in Fig. 2. In the forward region, the design of the preshower detector is presently under study. We had considered small angle tracking detectors, but eliminated them in favor of extended fiber barrels and small angle silicon disks due to cost considerations. The higher event rates in Run II have led us to add new muon trigger detectors covering the full pseudorapidity range. Electronic upgrades are driven by the need to handle a smaller bunch spacing and provide pipelining of the various front end signals from the tracking, calorimeter, and muon systems. The front-end electronics for all these systems will be replaced. The addition of new trigger elements and front-end electronics requires a new trigger control system.

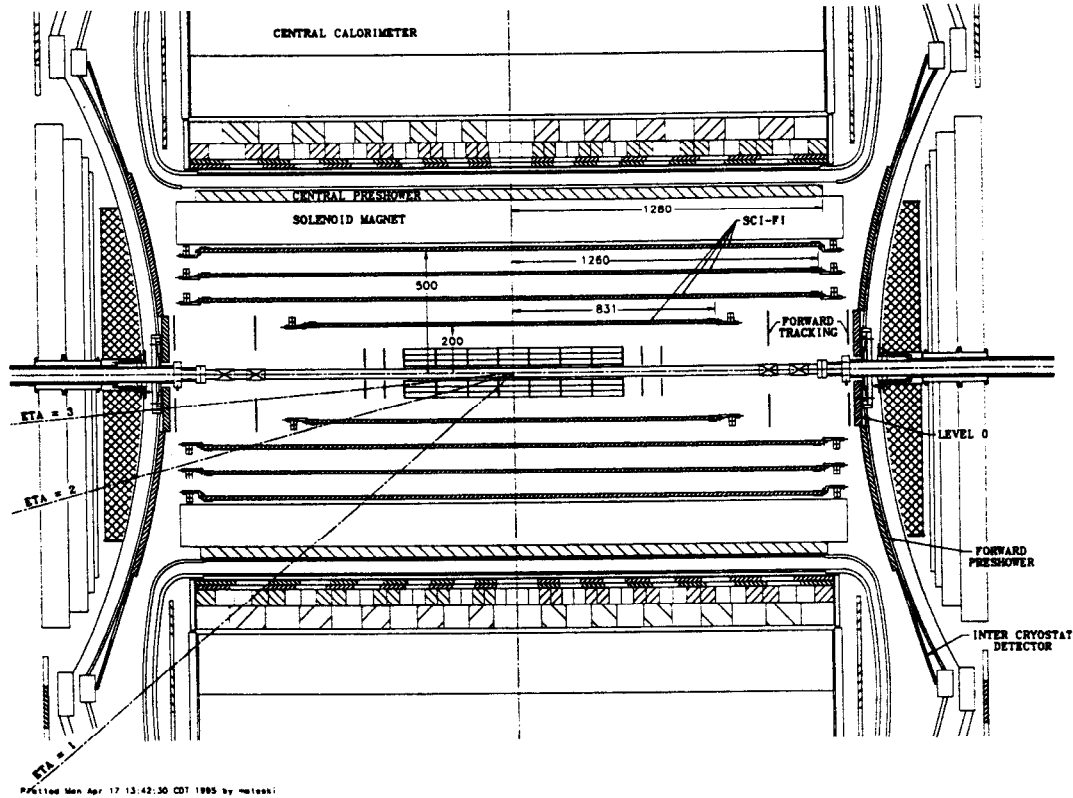


Figure 2. DØ tracking upgrade (dimensions in mm).

In Section 3, we summarize the physics capabilities of the DØ upgrade detector. The strengths of DØ are considerably enhanced in some areas of high  $p_T$  physics such as the ability to tag  $b$ -quarks in top decays using the silicon detector. Precision electroweak measurements such as the  $W$  mass measurement will benefit from the *in situ* energy calibration provided by electron momentum measurements. Some electroweak measurements that were previously impossible, such as the forward-backward  $Z$  decay asymmetry will be accessible with the addition of the magnetic field. The upgrades to the muon system and the addition of a silicon detector will improve our  $B$  physics capabilities by allowing triggering on low  $p_T$  muons and low mass dimuons and the reconstruction of complete  $B$  final states.

## 2. Description of the DØ Upgrade

### 2.1 The Solenoid Magnet

The momenta of charged particles will be determined from their curvature in the 2T magnetic field provided by a 2.8m long solenoid magnet. The superconducting (SC) solenoid, a two layer coil with mean radius of 60cm, has a stored energy of 5MJ (for reference the CDF coil is 30MJ). Inside the tracking volume the value of  $\sin\theta \times \int B_z dl$  along the trajectory of any particle reaching the solenoid is uniform to within 0.5%. This uniformity is achieved in the absence of a field-shaping iron return yoke by using two grades of conductor with higher current density near the ends of the coil. From the value of the field integral and the space point precision provided by the silicon and fiber tracking system,  $\Delta p_T/p_T^2 \approx 0.002$ . The SC coil plus cryostat is about 1.1 radiation lengths thick.

The solenoid is being built by Toshiba Corp. in Yokohama, Japan. They are under contract to provide the solenoid as specified by Fermilab. The contract was awarded in January 1995 and Toshiba presented its preliminary design to Fermilab in mid-March. Delivery of the magnet to Fermilab will occur in late 1996 after complete testing in Japan.

The cryogenic plant that supplies LHe for both the solenoid and the visible light photon counter (VLPC) readout devices is in the final stages of design and the initial stages of construction. After appropriate modifications to the DØ cryogenic services building, the Accelerator Division (AD) will provide the experiment with warm high pressure He. The expansion engines and heat exchangers, etc. used in making LHe, will be located in the DØ Assembly Hall. Modifications to the AD cryo building will begin in the 1995 summer shutdown.

### 2.2 The Silicon Vertex Detector

The tracking system was designed to meet several goals: momentum measurement with the introduction of a solenoidal field; good electron identification and  $e/\pi$  rejection (to compensate for the loss of the TRD); tracking over a large range in pseudorapidity ( $\eta \approx \pm 3$ ); secondary vertex measurement for identification of b-jets from top and for b-physics; second level tracking trigger; fast detector response to enable operation with a bunch crossing time of 132 ns; and radiation hardness. The silicon tracker is the high resolution part of the tracking system and is the first set of detectors encountered by particles from the collision.

Several of the Run II Collider machine parameters have an effect on the silicon design. The luminosity sets a scale for the radiation damage expected over the life of the detector, which in turn dictates the operating temperature ( $< 10^\circ\text{C}$ ). The long luminous region length sets the length scale, and motivates our hybrid disk and barrel design. The crossing interval sets the design parameters for the electronics and readout.

Since the Collider interaction point is extended, with a  $\sigma_z$  of 25cm, it is difficult to deploy detectors such that the tracks are generally perpendicular to detector surfaces for all  $\eta$ . This forced us to a hybrid system, with barrel detectors measuring primarily the  $r-\phi$  coordinate and disk detectors which measure  $r-z$  as well as  $r-\phi$ . Thus vertices for high

$\eta$  particles are reconstructed in three dimensions by the disks, and vertices of particles at small  $\eta$  are determined by the barrels.

The interspersed disk and barrel design is shown in Fig. 2. In such a system, the disk separation must be kept small to minimize extrapolation errors. However, each plane of disks also introduces a dead region between the barrels which lowers the overall efficiency of the detector. Thus there is a compromise between vertex resolution at large  $\eta$  ( $\approx 1/\text{disk spacing}$ ) and efficiency at small values of  $\eta$ . This design clearly puts a premium on minimizing the gap between barrel sections.

We have chosen the following overall geometry:

- 7 barrel segments in  $z$
- 4 detector layers per barrel
  - Layers 1 (innermost) and 3 are single-sided detectors (axial strips)
  - Layers 2 and 4 are double-sided detectors (axial strips and  $2^\circ$  stereo strips)
- 12 small diameter, double-sided “F” disks ( $30^\circ$  stereo)
- 4 large diameter, single-sided “H” disks ( $15^\circ$  stereo)

Table 1 shows the numbers of detectors and the geometric parameters of the tracker. The 12cm long barrel segments are separated by 8mm gaps containing F disks at  $|z| = 6.4\text{cm}$ ,  $19.2\text{cm}$  and  $32.0\text{cm}$ . Three more F disks are located at each end of the barrel at  $|z| = 44.8\text{cm}$ ,  $49.8\text{cm}$  and  $54.8\text{cm}$ . The H disks are located at  $|z| = 110\text{cm}$  and  $120\text{cm}$ .

### 2.2.1 Silicon Detectors

The barrels and the F disks are based on  $50\ \mu\text{m}$  pitch silicon microstrip detectors,  $300\ \mu\text{m}$  thick, providing a spatial resolution of approximately  $10\ \mu\text{m}$ . The small angle stereo design provides good pattern recognition with a resolution in  $r$ - $z$  at the vertex of  $0.5$ – $1.0\ \text{mm}$ , allowing separation of primary vertices due to multiple interactions. The detectors are AC coupled; each strip has an integrated coupling capacitor and a polysilicon bias resistor. This technology has been shown to be sufficiently radiation hard.<sup>[2]</sup> F disks are made from 12 double-sided detectors which have  $\pm 15^\circ$  stereo strips.

Results from tests of prototype F disks fabricated at Micron Semiconductor (UK) have shown that these detectors are suitable for use in DØ.<sup>[3]</sup> Leakage currents were  $< 120\ \text{nA/cm}^2$ ; coupling capacitors had a capacitance of  $> 20\ \text{pF/cm}$  and a breakdown of  $> 80\ \text{V}$ ; and the polysilicon resistance was  $> 3.5\ \text{M}\Omega$  with strip-to-strip non-uniformity of  $< 3\%$ .

Orders for all barrel detectors have been placed with Micron Semiconductor. The first pilot run (10 detectors) was completed on April 1, 1995 and we are currently evaluating these detectors. In a test beam run planned for April 1995 at TRIUMF we expect to re-verify radiation damage properties of the prototype F disk and barrel detectors.

The SVX II front end readout chips (see Sect 2.4) are mounted on a kapton high density circuit (HDI) which is laminated onto a  $300\ \mu\text{m}$  thick beryllium plate and glued to the surface of the detector. The end of the HDI consists of a kapton strip cable which carries signals and bias voltages to the outer radius of the detector ( $\approx 18\ \text{cm}$ ) where a connection to a long ( $\approx 8\ \text{m}$ ) low mass microstrip cable is made. These cables carry the signals to the

port cards located on the  $D\bar{O}$  support platform.

A prototype HDI has been designed and is in fabrication. However, due to delays in the manufacturing process we are actively seeking an alternate vendor and expect to procure and test the prototype by August 1995.

	F	H	L1	L2	L3	L4	TOTAL
# detector sides	2	1	1	2	1	2	
# assemblies (both ends)	12	4	7	7	7	7	44
R (min) (cm)	2.57	9.5	2.77	4.61	6.83	9.16	
R (max) (cm)	9.96	26	3.58	5.49	7.52	9.99	
z (min) or $\langle z \rangle$ (cm)	6.4	110	$\langle 12 \rangle$	$\langle 12 \rangle$	$\langle 12 \rangle$	$\langle 12 \rangle$	
z (max) (cm)	54.8	120	42	42	42	42	
# ladders/assembly	12	24	12	12	24	24	
Detector length (cm)	7.5	14.86	6	6	6	6	
Min detector width (cm)	1.673	2.42	2.115	3.395	2.115	3.395	
Max detector width (cm)	5.692	6.40	2.12	3.40	2.12	3.40	
Detector area (cm <sup>2</sup> )	27.62	65.53	12.72	20.4	12.72	20.4	
Strip pitch ( $\mu$ m)	50	50	50	50	50	50	
# IC's/side	8	10	3	5	3	5	
# detectors/readout unit	1	2	2	2	2	2	
# detectors/assembly	12	48	24	24	48	48	
# detectors (total)	144	192	168	168	366	366	1344
Silicon mass (g)	278	440	149	240	299	479	1885
Sides $\times$ area (cm <sup>2</sup> )	7954	7528	2137	6854	4274	13709	41222
# sets IC's/assembly	24	24	12	24	24	48	
# sets IC's	288	96	84	168	168	336	
# IC's	2304	960	252	840	504	1680	6540
# kchannels	294.9	122.9	32	108	65	215	837

**Table 1.** Numbers of detectors and geometric parameters of the tracker.

### 2.2.2 Mechanical support

The mechanical structure must provide a precise and stable support for the individual barrel and disk detectors, provide cooling for the heat generated in the SVX II chips and allow for the necessary cable paths for external connections. In the barrels, the basic mechanical unit is the ladder. Each ladder supports two detectors wire-bonded together, forming a 12 cm long unit with the SVX II readout at one end. A rohacell-carbon fiber support provides extra rigidity to the ladder. The ladders are mounted on beryllium bulkheads, which serve as a support at both ends of the ladder and provide cooling at the readout end by means of an integrated coolant channel.

The F disks are mounted in the 8 mm gap between the barrel segments. In analogy to ladders, disk modules consist of a single F disk detector with SVX II readout at the outer radius. Water cooling is via a beryllium cooling channel which also supports the modules at the outer radius.

The barrels and disks are mounted in a double-walled carbon half-cylinder which acts as a support with zero thermal expansion. The half-cylinder has a length of 2.2 m and an outer radius of 15.3 cm. As detector elements are installed, compensation will be made for the predicted 100  $\mu\text{m}$  half-cylinder gravitational deflection.

Designs completed in the mechanical systems include: the beryllium bulkhead and fabrication of prototype straight sections to test the cooling channel for leaks; the single-sided ladders, and the cooling system, including finite element analysis. Fabrication of a 10-inch long prototype half-cylinder support is complete.

### 2.2.3 Assembly and Testing

Barrel and disk modules will undergo thorough testing to avoid using modules with unacceptable fractions of dead channels. This will be done in stages, starting with probe testing of the individual silicon detectors and SVX II chips. Due to the large numbers involved, three sites have been set up with probe station facilities: Fermilab, UC Riverside and Oklahoma University. Further testing of HDI's instrumented with SVX II chips will be performed and, finally, the fully assembled ladders and disk modules will be checked with a 1064 nm wavelength laser, which simulates a charged particle track traversing the silicon.

Design and implementation of all assembly sequences and fixtures has been started. A detailed ladder fabrication sequence has been defined and a prototype ladder assembly fixture has been designed and fabricated.

### 2.2.4 Future Milestones

Some important milestones for the silicon tracker R&D and construction are given below.

- Test beam run at TRIUMF to verify radiation damage effects April 1995
- Fabricate and test 3- and 5-chip barrel detector prototypes May 1995
- Procure and test HDI prototype Aug 1995
- Radiation hard SVX-II submission Sept 1995
- Fabricate and test full ladder prototypes Oct 1995

- Fabricate and test full disk module Nov 1995
- Set up for test beam run with fully instrumented ladders May 1996

## 2.3 The Scintillating Fiber Tracker

A scintillating fiber tracker (CFT) surrounds the silicon vertex detector and covers the central pseudorapidity region. The fiber tracker serves two main functions. First, with the silicon vertex detector, the tracker enables track reconstruction and momentum measurement for all charged particles within the range  $\eta = \pm 1.7$ . Second, the fiber tracker provides fast, “Level 1” track triggering. Combining information from the tracker with the muon and preshower detectors, triggers for both single muons and electrons will be formed at Level 1. These triggers will be critical to take full advantage of the physics opportunities available with the Main Injector.

The scintillating fiber tracker is shown in Fig. 2. A total of about 80,000 scintillating fibers are mounted on four concentric cylinders with average radii of 20,30,40 and 50 cm. Each of the four cylinders supports a “superlayer” of four doublet fiber layers. Two of the doublet layers contain fibers oriented in the axial direction, parallel to the beam line. These two axial doublets are separated by the 1.5 cm thickness of the support cylinder. The other two fiber layers are oriented at  $\pm 1.5^\circ - 3^\circ$  stereo angles. All fiber doublet layers are constructed so that one layer is offset by one half of the  $\sim 900\mu\text{m}$  fiber spacing with respect to its partner. This configuration removes all gaps and improves the doublet position resolution. We have studied the tracking and triggering with Monte Carlo simulations and the expected performance is excellent.

### 2.3.1 Scintillating Fibers

The basic detection element is the multicladd scintillating fiber. The inner polystyrene core is surrounded by a thin acrylic cladding, which in turn is covered by a thin fluoro-acrylic cladding. These three materials have indices of refraction of 1.59, 1.49 and 1.42, respectively. The addition of the second cladding increases the light trapping by about 70% with respect to single-clad fibers, and improves the mechanical robustness of the fibers. The nominal fiber diameter is  $830\mu\text{m}$ ; the core diameter is  $770\mu\text{m}$  and each cladding is  $15\mu\text{m}$  thick. The polystyrene core is doped with 1% p-terphenyl (PTP) and 1500 ppm of 3-hydroxyflavone (3HF). The fiber scintillates in the yellow-green part of the visible spectrum, with a peak emission wavelength of 530 nm.

Eight meter clear multicladd fiber waveguides conduct the light to the photodetectors and are mated to the scintillating fibers by plastic, diamond-polished optical connectors. The photodetectors for the fiber tracker are placed in the platform under the central calorimeter.

### 2.3.2 Photodetectors

The photodetector must be capable of detecting single photons with high efficiency at high rates and with large gain. We will use the Visible Light Photon Counter (VLPC), a variant of the solid-state photomultiplier. Much research and development in collaboration with Rockwell International Corp. has led to a device with the characteristics: greater than 70% quantum efficiency for the wavelength of interest, gain of roughly 20,000, and a rate capability of at least 10 MHz. The VLPC can be operated at full efficiency with a noise rate of 0.1% or less. The VLPC's are manufactured in arrays containing 8 circular pixels each 1 mm in diameter, well-matched to the clear waveguide fibers. The photodetector operates with a bias voltage of about 7.5 volts. The VLPC's operate at a temperature of 6–8 K, requiring the detectors to be maintained in a cryogenic environment. Cryogenic "cassettes" are being designed which will house 128 arrays for a total of 1024 channels, and maintain them at a stable operating temperature.

### 2.3.3 Cosmic Ray Test Setup

The R&D program to develop the fiber system culminated in the operation of a large-scale scintillating fiber cosmic ray test stand at Fermilab. The test stand contained three 128-fiber-wide superlayers (a total of 3072 fibers). Superlayers were mounted at the top and bottom of a carbon-fiber support cylinder, with a third on a flat board on the cylinder axis. Muons with momenta greater than 2.5 GeV/c were selected using a steel filter. The cosmic ray setup was designed to test the major components of the fiber tracker in a configuration as close as possible to the final tracker design. The scintillating fibers were three meters in length, and were optically coupled to eight-meter-long clear waveguides. A cryostat was built to house test cassettes containing 128 VLPC channels each. The test stand was in operation from May through December 1994.

The results<sup>[4]</sup> of the cosmic ray test were excellent. The VLPC cryostat operated stably and the temperatures of individual cassettes were controlled to better than  $\pm 15$  mK, easily good enough for stable VLPC operation. The gain of each of the 3072 channels was monitored by an LED-based calibration system, and overall gains were found to vary less than 1% over the length of the run. The noise rate, which was fixed to 0.1% by setting thresholds on each VLPC channel, also remained constant over the entire run. The light yield and tracking resolution are consistent with expectations. Figure 3 shows the light yield spectrum in photoelectrons for all fibers found on tracks. The most likely value of 8.5 photoelectrons is about a factor of four more than the minimum required for efficient tracking. There was no evidence of any degradation in light yield over the duration of the run. The doublet hit efficiency for cosmic ray tracks is better than 99.9%. The doublet position resolution, plotted in Fig. 4, is found to be  $136\mu\text{m}$ .

### 2.3.4 R&D and Design

Currently, a variety of R&D tasks are being completed before construction of the fiber tracker begins. A new set of doublet ribbons with more accurate layer-to-layer registration has been manufactured and installed in the cosmic ray test stand and are expected to improve the position resolution to the theoretical limit of  $120\mu\text{m}$ . Designs for the fiber ribbon manufacture and for the optical connectors are being finalized. A joint Fermilab-Rockwell study to optimize the VLPC cassette design is near completion. Prototypes for the final calibration system are being tested, and alternative scintillating dyes which may prove superior to 3HF in speed and environmental stability are under investigation.

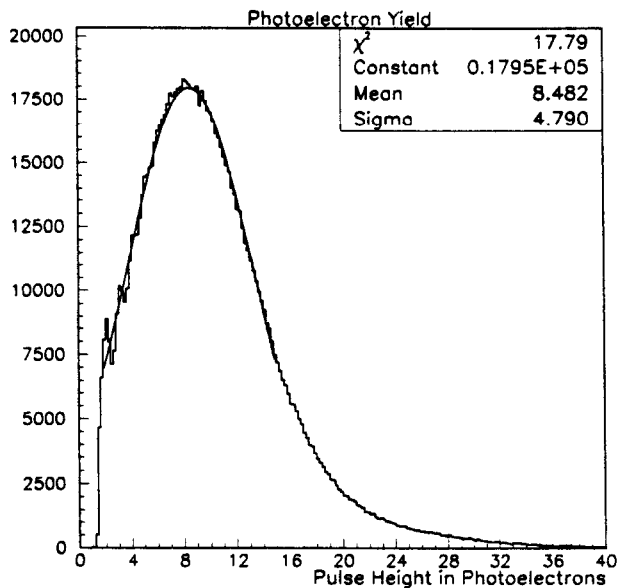


Figure 3. Light yield spectrum.

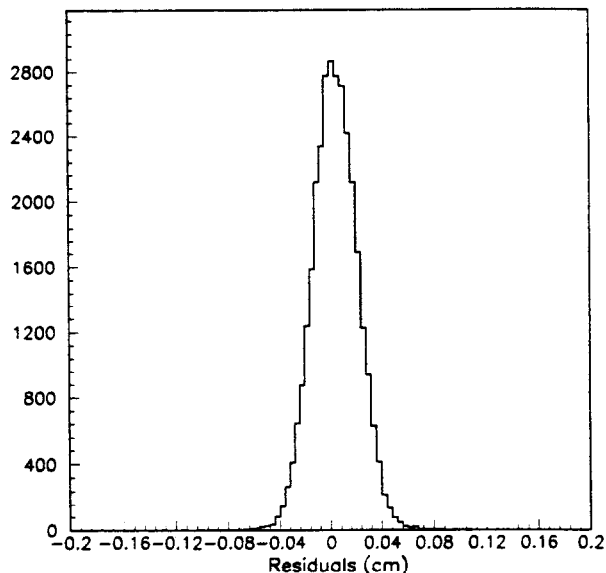


Figure 4. Fiber doublet position resolution.

## 2.4 Tracking Electronics

### 2.4.1 SVX II Chip

The readout for both the silicon vertex detector and the fiber tracker is based on the 128 channel SVX II chip developed by Fermilab and LBL. Each channel contains a double-correlated sampling charge sensitive preamp, 32 stages of analog pipeline delay, a Wilkinson 8 bit analog to digital converter and a sparse data readout system ( $< 5\mu\text{s}$  for  $\approx 3\%$  occupancy). The readout system employs a common digital threshold for all 128 channels. It also implements a 'nearest neighbor' readout scheme in which two channels below threshold neighboring a channel above threshold will also be read out. The chip is designed to accept data every 132 ns. At this crossing frequency, the 32 channel delay stage provides  $4.2\mu\text{s}$  for the Level 1 trigger decision. For the silicon tracking system, this chip is mounted directly on the detector. Two iterations of the SVX II chip have been prototyped in standard CMOS and tested. All parts of the chip are fully functional and the noise has been measured to be  $\sigma = 450e + 65e/\text{pF}$  for a risetime of 105 ns.

### 2.4.2 Silicon Readout

Figure 5 is a block diagram of the silicon readout system. The SVX II's are controlled by a readout card, called a port card, which is mounted in the detector platform. The silicon detector is connected to the port card by a 28 foot long metallic data path. The port card downloads the parameters to the SVX II chips, controls the chip during data taking, reads out the data after a Level 1 trigger and converts the data to optical signals and sends these signals over fiber optic cables to the moving counting house. It also provides temperature, voltage and current monitoring and some level of diagnostics. It generates the test pulse signal for the SVX II.

The optical signals are received in the Moving Counting House by the Silicon Acquisition and Readout board (SAR), a VME board that acts as a buffer for transferring data to the Level 3 system. Events are held in one of eight local buffers until a valid Level 2 accept is received, when they are sent to the existing VME buffer driver (VBD) for transmission to the Level 3 system. Level 2 rejects are discarded.

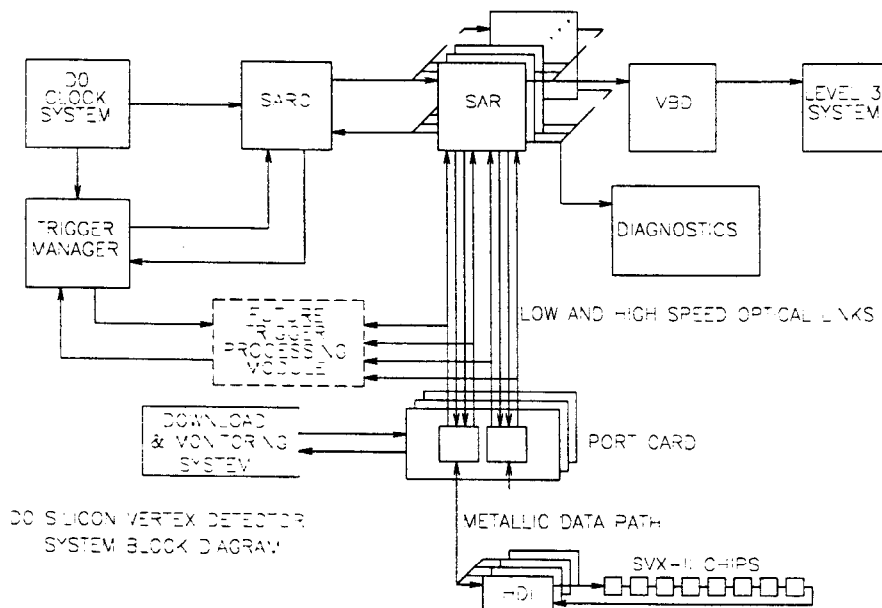


Figure 5. Block diagram of the readout system for the silicon detector.

### 2.4.3 Fiber Tracker Readout

The front-end electronics for the fiber tracker must provide a prompt Level 1 trigger pickoff, necessitating the development of a special 'precursor' chip between the VLPC and the SVX II. Each channel of this chip has a charge sensitive amplifier, a discriminator with TTL output and a buffer amplifier to put charge onto an output capacitor which is read by the SVX II chip. In order to prevent the chip from oscillating, the trigger is picked off with a different clock cycle than both the input and the transfer to the SVX II. The readout after the SVX II is nearly identical to that for the silicon system.

The trigger scheme for the fiber tracker is based upon the  $r-\phi$  hit patterns in 4.5 degree sectors and allows four distinct momentum thresholds. The output from the trigger pickoff chip is fed into a series of large Field Programmable Gate Arrays which are preloaded with the appropriate logic to form hits from the eight trigger layers. The FPGA's are static RAM, so thresholds are software settable. Trigger data is combined with the preshower detector on the trigger board and sent serially at 424 Mhz to other trigger systems.

## 2.5 The Preshower Detectors

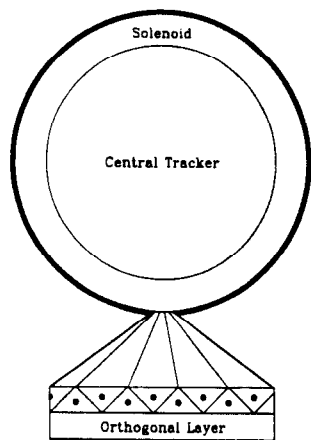
### 2.5.1 Central Preshower

The central preshower detector will aid electron identification and triggering and correct electromagnetic energy for effects of the solenoid. The detector functions as a calorimeter by early energy sampling and as a tracker by providing precise position measurements. The cylindrical detector will be placed in the 51 mm gap between the solenoid coil and the central calorimeter cryostat at a radius of 71 cm, and covers the region  $-1.3 < \eta < 1.3$ . The detector will consist of several layers of axial and stereo scintillator strips with a wavelength-shifting (WLS) fiber readout. An end-view of the detector for one of the designs described below is shown in Fig. 6. A lead absorber before the detector will be tapered in  $z$  so the coil plus lead yield two radiation lengths of material for all particle trajectories. The scintillation light from the preshower detector will be transported via clear light-guide fibers to the VLPCs. The readout is again based on the SVX II.

The fast energy and position measurements enable use of preshower information at the trigger level to aid electron identification. The axial layers of the preshower will be used in the Level 1 electron trigger. Monte Carlo studies show that the information from the preshower detector will provide a factor of five reduction in the low-energy trigger rate by applying a pulse height cut and requiring coarse position-matching with tracks. Off-line, the early sampling of the showers and the good position resolution of the detector will provide additional means for identifying electrons.

Two approaches for the scintillator strips are being considered. The first approach involves machining square scintillator strips, shown in Fig. 7(a), from large scintillator sheets. Six layers of strips will be arranged into  $z-z$ ,  $u-u$  and  $v-v$  views with a  $uv$  stereo angle of  $\pm 20$  degrees. The two layers in the same view will be staggered by a half-strip to reduce detector inefficiency. Each strip will be 5 mm thick and 5 mm wide. There will be 5760 channels in this design. The WLS fiber will be placed in a 'key-hole' groove at the center of the strip. A prototype module of this design was made and tested using the VLPC readout at the fiber tracker cosmic ray test facility at Fermilab. The module is

about one meter long and consists of 128 channels. With over 15,000 cosmic rays recorded per strip, the light yields, signal uniformity, attenuation length, edge effects and crosstalk were studied. The effective attenuation length is measured to be around 11 meter and a light yield of 4.5 photoelectrons per millimeter of scintillator traversed has been achieved for cosmic ray muons. The detailed prototype test results for this design are described in Ref. 5. The results show that there is a considerable margin in achieving the desired performance for the preshower detector.



(Beams eye view)

**Figure 6.** End-view of the central preshower detector with triangular strip inset.

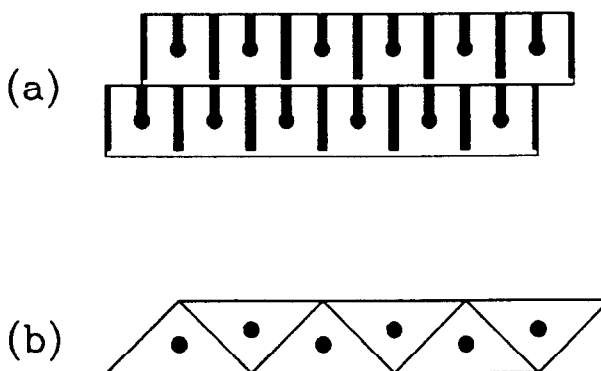


**Figure 7.**End views of (a) machined square strips and (b) extruded triangular strips.

The second option uses extruded triangular strips. Figure 7(b) shows the end view of this design. Triangular cells eliminate the need for two staggered layers of a square cross section, and therefore, make the detector more compact. In addition, this design improves the position resolution for minimum ionizing particles (MIP) as a result of light-sharing between two neighboring strips. We are considering a two-layer design of triangular strips. Each layer is 5 mm thick with a 5 mm fiber-to-fiber spacing. The inner layer will be arranged along the  $z$  direction. The outer layer will be arranged with the strips orthogonal to those of the inner layer. The channel count of this design is about 4000. A 128 channel module made of triangular strips is being tested at lab 6 for its optical viability.

Calibration of the detector will be done in two steps. Light emitting diodes (LED) will be utilized to provide a quick calibration on-line. Each non-readout end of the WLS fibers will be equipped with an LED. By comparing the one and two photoelectron peaks from the LED light, the relative calibration of the detector elements can be performed. An absolute calibration will be provided by MIP responses of the detector using the data. The Monte Carlo studies show that the MIP peak can easily be identified.

The optimization of the detector design is progressing well. The R&D effort is expected to be completed this summer and a final design will follow.

### 2.5.2 Forward Preshower

Two Forward Preshower Detectors (FPS) will cover the pseudorapidity regions  $1.4 < |\eta| < 2.5$ . They will consist of wedges joined together to form conical detectors mounted on the faces of the End Calorimeter (EC) cryostats. Each wedge will be composed of an inactive absorber material (two radiation lengths of lead) sandwiched between two finely-segmented active layers. The active layer before the absorber (layer 1) will serve as a track stub detector and the active layer behind the absorber (layer 2) will sample the showers initiated in the absorber.

The FPS will be part of the electron trigger in the forward region. At trigger Level 1, a spatial match between any hit in layer 1 and a hit with energy deposition larger than expected from a minimum ionizing particle in layer 2 can be formed. At trigger Level 2, such a pair of hits can be matched with a tower in the electromagnetic (EM) calorimeter with energy above a threshold. At Level 3, more sophisticated algorithms will match clusters in the FPS and EM calorimeter.

Particle level studies show that a matching resolution of 5 mm or better is required between FPS layers 1 and 2 to achieve a substantial reduction of the rate due to the accidental overlap of charged hadrons and photon showers. More detailed GEANT simulations are in progress to estimate the backgrounds due to early hadronic showers and to determine the optimal segmentation.

In the offline analysis, the FPS will provide additional rejection against backgrounds for electrons by providing a more precise spatial match between CFT or H disk tracks, FPS track-stubs and showers than the calorimeter could provide. This will be especially helpful in identifying electrons in busy environments, *e.g.* from  $b$  decays. The fine segmentation of layer 2 will allow resolution of showers initiated by a single photon and by two closely spaced photons from the decay of high  $p_T$   $\pi^0$ s.

The detector technology for the active layers has not been selected. We are considering two options: grooved scintillator sheets with optical fiber/VLPC readout or interpolating pad chambers. The scintillator solution would use the same technology as the Central Preshower Detector and will require no additional R&D effort, but would provide some constraints on the possible segmentation. A pad chamber could be segmented in any way but would require more bulky frames. The choice will be made on the basis of detailed GEANT studies, which will determine what segmentation is required to achieve the goals outlined above.

## 2.6 The Calorimeter System

The Calorimeter system upgrade is driven by the need to preserve the excellent performance of the calorimeter for Run II running conditions. For practical reasons, we have chosen not to make any modifications to the uranium liquid-argon calorimeter itself, but to restrict all the changes to the front-end electronics. One component of the calorimeter system that will need modification due to the effect of the solenoid field is the Intercryostat Detector (ICD), which uses phototube readout located in what is presently a field free region.

### 2.6.1 Calorimeter Front-End Electronics

An upgrade of the calorimeter front-end electronics is required because the minimum bunch crossing time will be reduced and the luminosity will be increased in Run II. The electronics upgrade will preserve as much of the existing infrastructure as possible.

To minimize the effects of pile-up in the calorimeter, we have re-optimized the shaping times. The present peak sampling time of  $2.2\mu\text{s}$  will be reduced to 400ns (matching both the charge drift times in the calorimeter and the expected minimum bunch-spacing at the start of Run II). Since this shorter shaping time increases the sensitivity to noise and reflections on the signal cables, we will replace the present cables from the calorimeter cryostat with cables that are impedance matched ( $30\Omega$ ) to both the cables inside the cryostat and the new preamp input impedance. The calorimeter signals are transported to preamps housed on the calorimeter. The present preamp hybrids will be replaced with new hybrids which will have better noise performance through use of dual low-noise FETs, and increased output drive capability in order to drive the long terminated-cable run from the preamp to shaper circuitry (baseline subtractor or BLS). The new preamps require new preamp motherboards and power supplies, but otherwise use the existing mechanical structure.

The shaper circuitry incorporates significant new elements in the design to provide the necessary pipelining of the calorimeter signals in order to provide time for a trigger decision to be made. The analog pipeline will use a switched capacitor array (SCA) originally developed for SSC work by LBL,<sup>[6]</sup> and modified to match  $D\bar{O}$  specifications. The SCA will sample the peak of the integrated charge signal from a preamp, shaped to provide a symmetric unipolar signal. The calorimeter signals require 12-bit accuracy with 15-bit dynamic range. This range requirement exceeds that which can be achieved with the SCAs, so a dual-pipeline will be used to accommodate the full dynamic range. To minimize the deadtime at high luminosity, the signals will be toggled between two dual-pipelines. Limiting the trigger to only one in a "superbunch" (a superbunch consists of 11 (or 33) bunches at 396 (or 132) ns spacing with about a  $2\mu\text{s}$  gap between superbunches) provides a deadtimeless system in which one of the dual-pipelines is reading out while the other is being filled with data. The gap between superbunches will provide a single baseline sample which will be used to remove long term drifts. The present BLS system (60,000 channels) will be fully replaced (including new power supplies, timing system, and pulser system) except for the mechanical infrastructure (crates, cabling, cooling, shielding).

The performance of the system with regard to pile-up has been simulated, and we find that the capability of the upgrade detector at high luminosity is comparable to that of the present detector at our present lower luminosities. Its performance at 132ns has also been checked and found satisfactory up to luminosities approaching  $10^{33}\text{cm}^{-2}\text{s}^{-1}$ .

The preamp design is finished and we anticipate completing the SCA R&D this year. A modest amount of R&D for the new timing and pulser systems should be completed by the beginning of next calendar year.

### 2.6.2 The Inter-Cryostat Detector

The Intercryostat Detector provides a single energy sample in the region between the Central and End Calorimeter cryostats. This sample serves to improve the detector performance significantly in the overlap region  $1.1 < |\eta| < 1.4$ . The solenoidal field will render the present ICD phototube readout inoperable. Thus the upgrade of this detector system consists of modifying the present scintillator-tile system with waveshifter and fiber readout by moving the phototubes to a lower magnetic field environment. This will preserve the present capabilities of this system.

## 2.7 The Muon System

The advent of the Main Injector requires a major redesign of the DØ muon system triggering and front-end electronics systems. Bunch crossing times of 396 and 132 nsec are smaller than the drift time of the wide angle muon system (WAMUS) and the 132 ns time is less than that of the small angle system (SAMUS). The chambers will be preserved but the existing readout electronics will be replaced. In addition, it is necessary to improve the rejection power of the muon trigger systems considerably in order to handle the factor of ten increase in luminosity.

The WAMUS chambers are extruded aluminum tubes with a rectangular cross section. The wires are 50  $\mu\text{m}$  gold clad, nickel struck tungsten. The drift distance is 5 cm with field shaping electrodes made of "glassteel" in a pattern such that the relative charge on two adjacent triangular pads yields a coordinate along the wire direction. The SAMUS chambers are stainless steel tubes with a diameter of 3.2 cm. There is no field shaping, and only drift time is recorded. A three-dimensional readout is achieved by using crossed  $x \times y \times u$  tubes. WAMUS covers  $|\eta| < 2.4$  while SAMUS covers  $2.4 < |\eta| < 3.4$ . The detectors are organized in three layers; the A layer for WAMUS is located between the calorimeter and the toroid iron, the B and C layers are located outside the toroids, with the C layer outermost. This notation is built into the acronyms in the discussion that follows.

We will use the existing high voltage, low voltage, gas systems, and coaxial-cable runs to the moving counting house (MCH) and the L2 trigger system. The L1 trigger system will be moved to the detector platform and use new serial data links, greatly simplifying the trigger cable plant. As much of the existing infrastructure will be reused as is possible.

### 2.7.1 Muon Front-End Electronics

The front-end electronics for the muon system must be replaced to accommodate the shorter bunch-crossing times. Improvements in available electronics make it possible to replace the present discrete-component systems with commercially available integrated circuits.

The chamber wire signals will be processed by new amplifiers with transformer coupling at the inputs to avoid low impedance ground paths between the chambers and the preamplifier inputs. These commercial-IC based preamplifiers will provide equivalent noise performance to that achieved in the present run. The trigger information will be provided by wire signal latches, with the ambiguities, caused by the "ganging" of pairs of tubes,

resolved by inserting a lumped delay between the adjacent tubes.

The time digitizers use a KEK-developed four-channel pipelined digital TDC chip called a TMC<sup>[7]</sup> which matches our needs very closely. The bin width when run at 26 MHz is 1.2 ns and the maximum delay is 4.8  $\mu$ s, enough to cover the first level trigger (L1) latency of DØ of 4.1  $\mu$ s. The time-of-arrival difference between each end of the tube pair signals is used to break the ambiguities of the repetitive pad pattern. We propose to calculate  $\Delta t$  by subtracting time values from adjacent tubes.

The charge will be measured using a commercial 500 ns gated integrator, and digitized by a 10-bit 15-Msps ADC. The ADC signals are pipelined to provide deadtimeless L1 operation. This will allow us to maintain 2 mm pad resolution from 1% measurements of the individual pad pulse heights.

In order to form a trigger using the complete hit map for a particular collision, the signals cannot be used until the maximum drift time has elapsed. Thus the wire signal must be stretched to the maximum drift time, which is greater than the crossing interval. The problem of correlating hits with their corresponding collision can only be accomplished with the previously mentioned auxiliary detectors.

The rate capabilities of the data acquisition system (DAQ) dictate a hierarchal trigger scheme. In the muon system, which uses the TMC chip, the L1 pipeline is integral to the chip. The trigger logic generates a new candidate list of hits at a 53/7 MHz rate. The need to send trigger bits to the L1 processor at this speed defines its bandwidth requirements, which can be handled by serial links with rates as high as 1 Gbit/s developed for telecommunications. These serial links will be used to transmit signals to the L1 trigger and to the L2/DAQ in the counting house.

For the ADCs, we must supply an external pipeline. The present plan is to use a FIFO as a pipeline to provide at least eight-deep buffers. The outputs of the L1 FIFOs are attached to a data bus controlled by a digital signal processor (DSP). This high level processor will perform data formatting, including pedestal subtraction, and time to distance conversion, and more extensive processing depending on the high level processing algorithm.

### 2.7.2 Muon Trigger Detectors

Since the bunch crossing time for Run II will be smaller than the WAMUS (SAMUS) drift time of 700 (200) ns, subsidiary detectors are required to remove the ambiguities and to provide the "time stamp" for the event. The muon trigger detectors consist of:

- scintillator for the wide angle region (CF) cosmic ray shield for  $0 < |\eta| < 1$ ,
- scintillator counters located on the inner layers of the wide angle region (CFA) for  $0 < |\eta| < 1$ ,
- fast PWC "pad pixel" chambers for  $1 < |\eta| < 2.3$  (EF region),
- scintillator "pixel" trigger counters in the region  $2.3 < |\eta| < 3.3$ .

The cosmic ray shield was completed and brought into operation during Run Ib. The readout for all these detectors is designed. They will be part of the muon system data stream, reporting to L1 and L2/DAQ.

The experience gained from data taken in Run Ia was invaluable for learning how to operate a muon trigger in the Tevatron environment. In particular, the forward region is very susceptible to albedo from the End Calorimeters and the low-beta aperture stops. Prototype scintillators and pad-pixel chambers have been installed in the present experiment yielding the rates, pulse heights and timing spectra which are required for the upgrade design. Shielding studies have led to reduced rates which are of critical importance to triggers based on a three-element coincidence.

We have found that the effective rate can be reduced in both EFB and EFC by a factor of 50 by using 20 nsec timing gates to reject albedo. Similar factors are measured for CFA scintillator. We are also measuring the reduction of rates due to soft photons, obtained by using pulse height cuts on the scintillator signals. Clearly, scintillator is the detector of choice, but its use is constrained by the total system cost. We are optimizing the cost/benefit to establish the transition point between scintillator and PWC detectors on the basis of measurements taken in Run Ib. The time to freeze the design is the summer of 1995.

## 2.8 Trigger Systems

The present  $D\bar{O}$  triggering system includes two hardware triggers Level 0 (L0) and Level 1 (L1), and a Level 3 (L3) software trigger.\* Interactions with coincident hits in the small angle counters on both sides of the interaction region give a L0 trigger. After a L0 accept, the L1 trigger requires either a minimum  $E_T$  deposition in the calorimeter or primitive tracks of minimum  $p_T$  in the muon chambers. Once an event passes the L1 trigger, the entire detector is read out and the event assembled in a farm of VAX computers. This farm, the L3 trigger, performs a nearly complete reconstruction of the event. If the event includes objects of sufficient interest, it is written to tape. Between L1 and L3, a third hardware trigger (L2) refines the calorimeter-based trigger for electron candidates by examining the shape of the energy deposition, and refines the muon trigger by using finer granularity hardware information. L2 presently interrogates only a subset of the L1 accepts and inhibits data taking while examining the event. Typically, this limits the current L1/L2 accept rate to 150 Hz. The maximum L3 accept rate is 4 Hz.

A typical Run I trigger menu includes high  $p_T$  jet, electron, muon and large missing  $E_T$  triggers. The L1/L2 and L3 cross-sections, at a luminosity of  $2 \times 10^{32} \text{cm}^{-2} \text{s}^{-1}$ , are 10 and  $0.05 \mu\text{barns}$ , respectively. These correspond to trigger rates of 2000 Hz for L1/L2 and 10 Hz for L3 at  $2 \times 10^{32} \text{cm}^{-2} \text{s}^{-1}$ , which are beyond our present capabilities. In order to deal with these high rates, the  $D\bar{O}$  triggering system requires significant enhancement. The upgrade must include a new trigger framework to deal with the increased rates and several new triggering elements, including the fiber track trigger (CFT), the central preshower trigger (CPS), the forward preshower trigger (FPS), and muon trigger detectors, to provide the necessary rejection of background.

The present L0 provides a trigger and luminosity measurement. The magnetic field requires that the L0 system be replaced because of its conventional phototube readout.

---

\* We have replaced the existing  $D\bar{O}$  nomenclature of L0, L1, L1.5, and L2.

The luminosity monitor functions will be replaced by the new L0 system.

### 2.8.1 The Trigger Framework

There are two distinguishing characteristics of the new framework. First, all events will be examined by L2 hardware engines – not just a subset of events. Second, there will be event buffers between L1 and L2 and between L2 and L3. The addition of eight buffers between each trigger stage de-randomizes the Poisson distributed arrival times of the events, decreasing deadtime due to pileup. The buffers also eliminate the present L1 disable during L2 operation. These two improvements alone increase the L1 accept rate to 5-10 kHz and the L2 accept rate to 800 Hz. Since the Run II event sizes will be half that of Run I, an 800 Hz event transfer rate to L3 and a 10 Hz rate to tape are feasible. In summary, the expected Run II trigger accept rate limits are 10 kHz, 800 Hz, and 10 Hz at L1, L2, and L3, respectively.

### 2.8.2 Level 1,2 and 3 Trigger Systems

The L1 high-transverse-momentum electron trigger will be upgraded from the simple threshold in  $E_T$  to include a CFT track and CPS deposition for  $|\eta| < 1.2$ . The CFT momentum threshold gives good rejection against minimum bias (QCD) background. Requiring an energy deposition in the CPS which matches spatially with the track further improves rejection against isolated charged pions. Since the calorimeter L1 trigger does not contain spatial information, it cannot be used to further improve the background rejection. The forward electron trigger will use the calorimeter, as before, and the new forward preshower. The L1 high  $p_T$  trigger rate will be  $\sim 1000$  Hz at  $2 \cdot 10^{32} \text{cm}^{-2} \text{s}^{-1}$ .

Both the forward and central L2 electron triggers will retain the present electron isolation and shape requirements. In addition, a rejection factor of approximately two should be possible by requiring a coincidence among the calorimeter, CFT, and CPS in the central region and between the calorimeter and the FPS in the forward region. With these new elements, the L2 electron trigger rate at  $2 \cdot 10^{32} \text{cm}^{-2} \text{s}^{-1}$  will be  $\sim 200$  Hz for  $E_T > 15$  GeV. A L3 electron rejection factor of 100 can be achieved by importing current off-line shape cuts into the software farm; the high-momentum electron rate at  $2 \cdot 10^{32} \text{cm}^{-2} \text{s}^{-1}$  will be  $\sim 2$  Hz for  $E_T > 20$  GeV.

The L1 high  $p_T$  central muon triggers ( $|\eta| < 1.6$ ) will also incorporate the CFT. Coincidences between the CFT and the inner-layer muon scintillators, and/or the muon chambers themselves, will provide substantial background rejection. The forward ( $2 < |\eta| < 3$ ) muon triggers will rely on the A, B, and C pixel layers and SAMUS coincidences. Additional shielding, multiplicity cuts, multiple interaction cuts and pulse height discrimination will reduce the rates further. At the lowest  $p_T$  (1.5 GeV), a pair of CFT • A-layer  $\phi$  coincidences will serve as a di-muon or  $J/\psi$  trigger. A Level 2 di-muon mass trigger could provide rejection factors of five for a  $J/\psi$  trigger. The high  $p_T$  L1 muon rate at  $2 \cdot 10^{32} \text{cm}^{-2} \text{s}^{-1}$  will be  $\sim 200$  Hz. The goal is to trigger on one muon with  $p_T^\mu > 8$  GeV unprescaled, and on two muons for  $p_T^\mu > 2 - 3$  GeV. Measurements and extrapolations based on data and Monte Carlo calculations indicate that this is possible.

Changes in the trigger framework and the addition of triggering elements will meet the high rate demands of Run II. Table 2 is a summary of the L1, L2 and L3 rates for various

generic triggers at  $2 \cdot 10^{32} \text{cm}^{-2} \text{s}^{-1}$ . For completeness, high  $p_T$  jet, photon, and missing  $E_T$  triggers have been included. Note that there is sufficient bandwidth for more specific low rate top, di-lepton and tri-lepton search triggers.

Trigger	L1 (Hz)	L2 (Hz)	L3 (Hz)
Capability	5-10k	800	10
High $p_T$ electrons	1000	200	2
High $p_T$ muons	250	250	3
Central Di-muon	500	100	1
High $p_T$ jet	80	40	1
High $p_T$ photon	30	10	1
High missing $E_T$	140	140	1
Total trigger rate	2000	740	9

**Table 2.** Approximate Run II trigger capabilities and accept rates for high  $p_T$  physics.

## 2.9 Data Acquisition and Computing

The data acquisition architecture for  $D\bar{O}$  in Run II, as illustrated in Fig. 8, will be largely unchanged from the current system. The basic components will remain: VME Buffer Drivers (VBDs) in each front end electronics crate driving one of eight parallel high-speed Data Cables feeding Multi-Port Memories (MPMs) accessed by a farm of event-building and software-filtering Level 3 processor nodes with another VBD - Data Cable system feeding event data-logging and monitoring host cluster.

The VBD - Data Cable - MPM path will handle a rate of 160 Mbytes per second ( $\sim 800$  Hz) to the Level 3 processor farm using existing components. The 48 Level 3 nodes will be replaced with ones running an open operating system, i.e. one which will provide the necessary real-time functions yet will allow great flexibility in choice of commercial hardware. An example Level 3 system in current terms might be a PCI-based PC running Windows NT. The processor farm must possess sufficient compute capacity to provide a software trigger rejection factor of approximately eighty by executing a substantial subset of the current offline algorithms.

The VBD - Data Cable - MPM path from Level 3 to the host system will be designed to accommodate a rate of 5 Mbytes per second ( $\sim 20$  Hz). The host system is also to be assembled from commercial components. Incoming event data will be written to local disk buffers for later spooling to local or remote serial media. The host system will also provide the platform for monitoring of the data stream and will act as the interface to the hardware monitoring and control system.

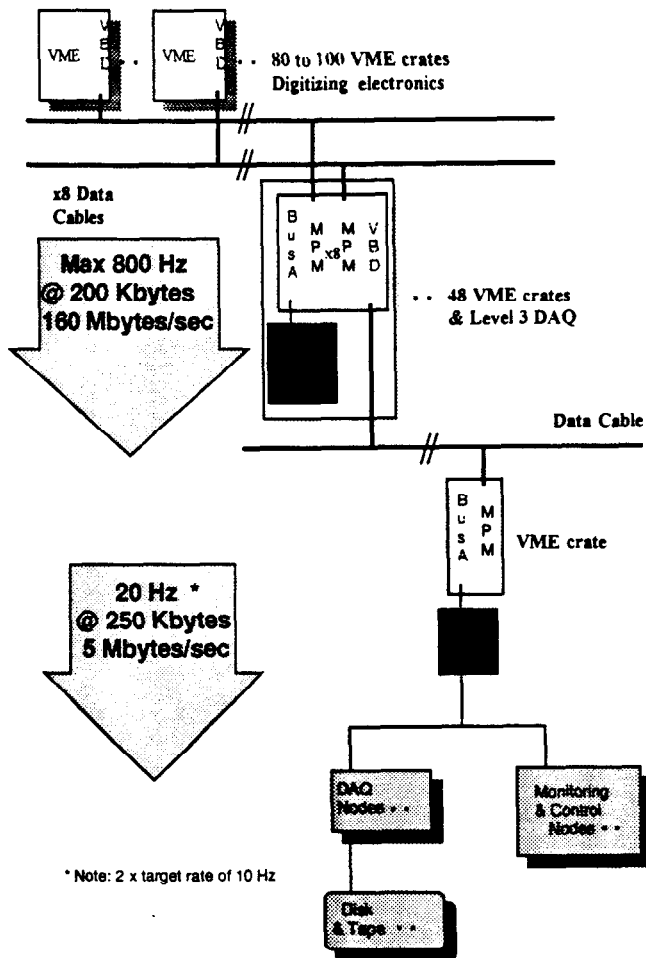


Figure 8. Upgrade Online computing architecture.

Events will be reconstructed on the FNAL processor farm system, with that portion dedicated to  $D\bar{O}$  (an estimated 20,000 MIPs) capable of matching the 10 – 20 Hz data acquisition rate. Following reconstruction, data will be stored on a tightly coupled disk and robotic tape system, and made available for analysis on a centralized analysis processor. We expect ~ 250 million events per year to be accumulated, requiring 3 Tb disk-resident and 160 Tb tape-resident storage.

### 3. Physics Topics and Detector Performance

#### 3.1 Introduction

The present  $D\bar{O}$  detector has proved to be an extremely powerful instrument for the study of the standard model (SM). Its finely segmented calorimeter and large angular coverage for electron and muon identification and measurement have enabled a wide range of physics studies to be addressed. A recent highlight was the announcement of the observation of the top quark by  $D\bar{O}$  in March.<sup>[8]</sup> The goals of the  $D\bar{O}$  upgrade are, firstly, to maintain this excellent performance in the future Main Injector era, when the Tevatron luminosity will be increased by a factor of 10 from today and the bunch spacing reduced from the present  $3.6 \mu\text{s}$  to  $396 \text{ ns}$  (and eventually  $132 \text{ ns}$ ); and secondly to significantly extend the capabilities of the detector. In particular we will:

- tag  $b$ -quark decays using displaced vertices in the silicon tracker;
- enhance muon identification and triggering, especially at low  $p_T$ ;
- enhance electron identification and triggering using the preshower and central tracking detectors;
- determine the charge of electrons and positrons.

The improved momentum measurement capabilities of the upgraded  $D\bar{O}$  detector are shown in Fig. 9.

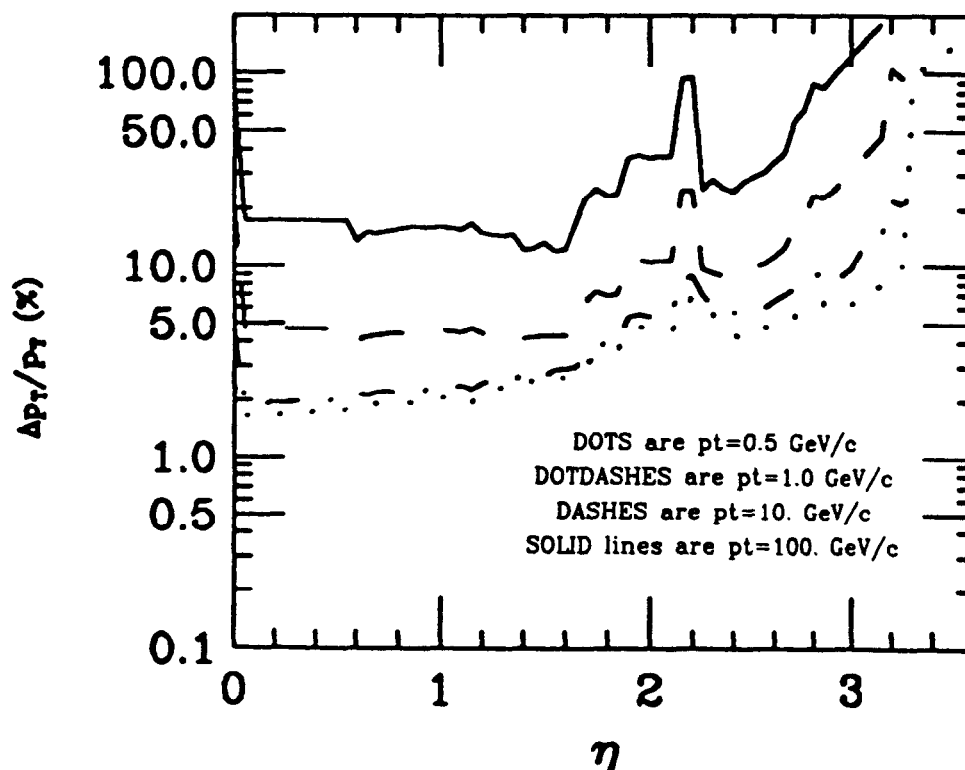


Figure 9. Charged particle momentum resolution *vs*  $\eta$  for various  $p_T$ 's.

In the following sections, we discuss some of the many physics topics which the upgraded detector will address. The program will be much richer than the outline given here, and we expect to further refine our analyses in the light of experience to achieve improved precision. The overall themes of the upgrade physics program are to seek the mechanism of electroweak symmetry breaking, through the study of large samples of the top quark and precision measurements of the parameters of the standard model; to make precision tests of the color force using a variety of probes and measurements in new regions of phase space; to carry out a broad programmatic study of  $b$ -quark hadrons; and to search for physics beyond the current paradigm.

## 3.2 Top Physics

### 3.2.1 Run I Observation of the Top Quark

Recently  $D\bar{O}$  published<sup>[8]</sup> an analysis based on data with integrated luminosities between 44 and 56  $\text{pb}^{-1}$ , depending on the channel. We observed a top quark signal in both dilepton and single-lepton channels. The dilepton candidates possessed two isolated leptons, at least two jets, and large missing transverse energy  $\cancel{E}_T$ ; the single-lepton candidates had one isolated lepton, large  $\cancel{E}_T$ , and a minimum of three jets (with muon tag) or four jets (without tag). We imposed a minimum requirement in all channels on  $H_T$ , the scalar sum of the transverse energies  $E_T$  of the jets (for the single-lepton and  $\mu\mu + \text{jets}$  channels) or the scalar sum of the  $E_T$ 's of the leading electron and the jets (for the  $e\mu + \text{jets}$  and  $ee + \text{jets}$  channels).

For the dilepton channels, the main backgrounds arise from  $Z$  and continuum Drell-Yan production ( $Z, \gamma^* \rightarrow ee, \mu\mu$ , and  $\tau\tau$ ), vector boson pairs ( $WW, WZ$ ), heavy flavor ( $b\bar{b}$  and  $c\bar{c}$ ) production, and backgrounds with jets misidentified as leptons. For the single-lepton channels, the main backgrounds are from  $W + \text{jets}$ ,  $Z + \text{jets}$ , and multijet production with a jet misidentified as a lepton. From all seven channels, we observed 17 events with an expected background of  $3.8 \pm 0.6$  events.

Our measured cross section as a function of the top quark mass hypothesis is shown in Fig. 10.

Assuming a top quark mass of  $199 \text{ GeV}/c^2$ , the production cross section is  $6.4 \pm 2.2 \text{ pb}$ . The error in the cross section includes an overall 12% uncertainty in the luminosity. The probability of an upward fluctuation of the background to 17 or more events is  $2 \times 10^{-6}$ , which corresponds to 4.6 standard deviations for a Gaussian probability distribution. We have calculated the probability for our observed distribution of excess events among the seven channels and find that our results are consistent with top quark branching fractions at the 53% CL. Thus, we observe a statistically significant excess of events and the distribution of events among the seven channels is consistent with top quark production.

To measure the top quark mass, single-lepton + four-jet events were subjected to 2-constraint kinematic fits to the hypothesis  $t\bar{t} \rightarrow W^+W^-b\bar{b} \rightarrow \ell\nu q\bar{q}b\bar{b}$ . With the  $H_T$  requirement removed and additional kinematic requirements loosened, allowing a substantial background contribution at lower mass, 27 single-lepton + four-jet events remained of which 24 were fitted successfully. An unbinned likelihood fit, incorporating top quark and background contributions, with the top quark mass allowed to vary, was performed on the

fitted mass distribution. The background contributions were constrained to be consistent with our background estimates, but the result of the fit did not change significantly when the background normalization was left unconstrained. The best fit top quark mass was  $199^{+19}_{-21}$  (stat.)  $\text{GeV}/c^2$ . This is consistent with the result obtained from the standard event selection. The total systematic error is  $22 \text{ GeV}/c^2$ , dominated by the uncertainty in the jet energy scale.

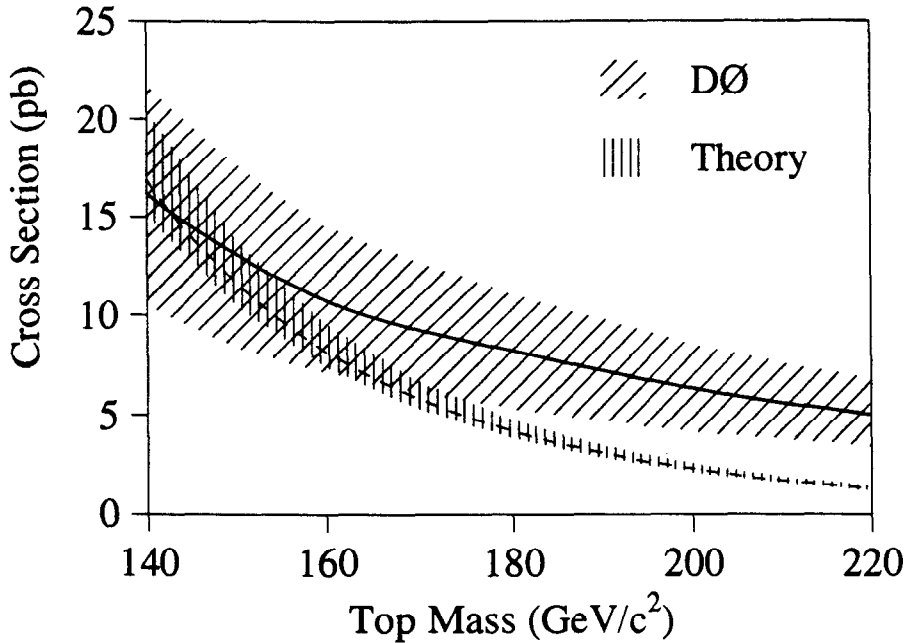


Figure 10. DØ measured cross section for  $t\bar{t}$  production as a function of  $t$  mass.

### 3.2.2 Run II Detector Improvements for Top Physics

#### 3.2.2.1 Lepton $p_T$ resolution

All simulations described here for top physics include detailed ISAJET/GEANT modeling of radiative effects and interactions in material, etc., and use full pattern recognition of tracks with raw hits as input. These simulations yield a  $p_T$  resolution for magnetic tracking of electrons from  $t \rightarrow e$  ( $t \rightarrow b \rightarrow e$ ) of  $0.002p_T^2$  ( $0.003p_T^2$ ). This is independent of and in addition to the  $\approx 0.15p_T^{1/2}$  resolution available both in Runs I and II from the central electromagnetic calorimeter. With the calorimeter continuing to provide the best information above  $p_T \approx 20 \text{ GeV}/c$ , the main advantages of magnetic tracking for electrons lie in new capabilities for triggering and for electron identification using  $E/p$ , and in identification of the electron charge.

The benefits of magnetic tracking within the central volume enclosed by the calorimeter are dramatic for muons, which will enjoy slightly better momentum resolution from the solenoid than do the electrons. In Run I the muon  $p_T$  resolution is bounded at low  $p_T$  by  $\approx 0.2p_T$  due to Coulomb scattering in the steel filter. At high  $p_T$  it is limited to  $\approx 0.003p_T^2$  by muon drift chamber resolution including alignment. With the addition of central magnetic

tracking in Run II, the muon  $p_T$  resolution will improve by a factor of about two at high  $p_T$ . At lower  $p_T$  the muon resolution will improve even more, by a factor of approximately  $100/p_T(\text{GeV}/c)$ .

### 3.2.2.2 Lepton tagging of $b$ from $t$

In Run II the new muon A-layer counters will permit muon identification and momentum reconstruction down to  $p_T \approx 1.5 \text{ GeV}/c$ . This will extend acceptance for soft muon  $b$  tags well below the present  $\approx 4 \text{ GeV}/c$ . Triggering on all top final states containing such tags (dilepton, lepton+jets, and all jets) will be enhanced by the new ability in Run II to trigger on muons above 6–10 GeV over most of the  $\eta$  acceptance of the calorimeter. This will become possible owing to the new dedicated muon trigger counters.

The new preshower detector, combined with the  $E/p$  match afforded by magnetic tracking, will allow  $D\bar{O}$  in Run II to carry out  $b$  tagging in the electron channel as well. Preliminary studies indicate that the fine segmentation of the EM calorimeter permits soft electrons from  $b$ -decays to be found with good efficiency ( $\gtrsim 50\%$ ). The preshower and  $E/p$  match will serve to reduce the presently large backgrounds.

### 3.2.2.3 Lifetime tagging of $b$ from $t$

We have studied  $b$  jet tagging in  $t\bar{t}$  events using a simple signed impact parameter technique. First we generate 638  $t\bar{t}$  ( $t \rightarrow b\nu$ ) events ( $m_t=160 \text{ GeV}$ ) imposing no restrictions on the composition of the  $b$  jets. As usual these events were fully GEANT simulated and pattern recognized although, conservatively, only the barrel silicon and fiber detector hits were used. Each reconstructed track was then associated with one ISAJET jet based on a cone cut of 0.45 in  $\eta - \phi$  space.

The distributions of signed impact parameter  $\delta$  and of its significance for all tracks associated with  $b$  jets in both  $t\bar{t}$  events and QCD jet events were studied. The distribution of  $\delta$  for tracks associated with  $b$ 's is found to be comparable in these two samples. Likewise, the distribution of  $\delta$  for tracks in non- $b$  jets in the top events (from the  $W$  from  $t$  decay) was found to be comparable to that for tracks with zero decay lifetime in QCD dijets. This assures us that our Run II tracking resolutions will not be significantly degraded in busier events with larger total  $p_T$ .

Using the  $W$ +jets simulation program VECBOS, with supplementary QCD evolution and hadron fragmentation performed by ISAJET, we also produced a 100 event background sample. Thereafter both the top and  $W$ +jets events were simulated and reconstructed identically. To obtain a first estimate of performance, we considered a jet to be  $b$  lifetime tagged if at least three of its tracks possessed a (positive) impact parameter significance of at least  $3\sigma$ . By itself, this requirement preserved more than 50% of the top signal events, while eliminating all but  $2 \pm 1.4\%$  of the  $W$ +jets background. As displayed in Fig. 11, further requiring the minimum tagged jet  $E_T$  to exceed 30 GeV reduced the background to  $1 \pm 1\%$  while retaining 46% of the original top signal. We emphasize that these performance figures are a conservative first estimate made with a very simple algorithm. No cuts, for example on the longitudinal event vertex position, were made especially for this study.

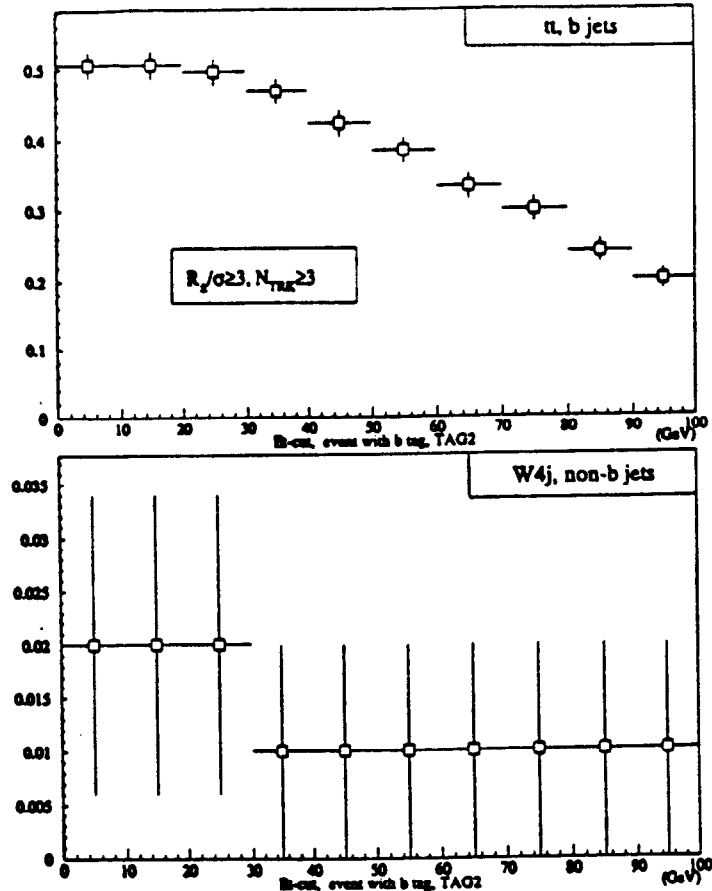


Figure 11. Tagging efficiency per event, as a function of the minimum required jet  $E_T$ , for (a)  $t\bar{t}$  signal events and (b)  $W + jets$  background.

### 3.2.3 Run II Top Analysis and Expected Precision

The following assumes an integrated luminosity to tape of  $2 \text{ fb}^{-1}$  delivered to the upgraded  $D\bar{O}$  detector. We consider a center of mass energy limited to the present  $\sqrt{s}=1.8$  TeV (though raising it to 2.0 TeV would increase the yields by 30%). We normalize to the measured background subtracted top event rate, which corresponds to a cross section for 200 GeV top of 6.4 pb. For simplicity, where appropriate we apply the same “standard” cuts recently used for our initial top quark observation.

#### 3.2.3.1 Pair production of $t\bar{t}$

Addition of the silicon tracker will open a fourth ( $b$  lifetime tagged lepton+jets) channel for  $D\bar{O}$ 's top analysis, in addition to the dilepton, soft  $\mu$  tagged lepton+jets, and shape

selected lepton+jets modes used in Run I. Compared to the presently available channels, the  $b$  lifetime tagged sample will have nearly the highest top acceptance combined with the second lowest background.

Further improvements in Run II top analysis will include a factor of two reduction in dilepton background from the electron sign selection and the more precise rejection of  $Z \rightarrow \mu\mu$ , and an increase in soft  $\mu$  tagging efficiency from the lower muon  $p_T$  threshold.

Together the Run II improvements will make possible an increase from  $\approx 0.3/\text{pb}^{-1}$  to  $\approx 0.5/\text{pb}^{-1}$  in the yield of background subtracted top events passing final cuts, without any corresponding background increase. With an integrated luminosity of  $2 \text{ fb}^{-1}$ , we expect a final sample of  $\approx 1000$  background subtracted top candidates with signal to background  $\geq 5:1$ . Either the yield or the S:B, and probably both, can be enhanced by further optimization of the cuts and selection algorithms. With these statistics, the error on the measured top cross section clearly will be dominated by systematics.

### 3.2.3.2 Top quark mass

A  $W$  mass precision approaching  $\approx 35 \text{ MeV}$  may be achieved shortly after the end of the decade from the Tevatron and LEP200 experiments. Our goal is to measure the top mass in  $D\bar{O}$  to a precision of  $5 \text{ GeV}$ , or  $2.5\%$ . The sensitivity of the Higgs mass to  $m_t$  and  $m_W$  is such that an error on the top mass much larger than this will dominate the uncertainty on  $m_H$ , while smaller errors on  $m_t$  do not significantly improve the precision with which  $m_H$  is constrained. Our  $5 \text{ GeV}$  goal corresponds to a Higgs mass uncertainty of  $\delta m_H/m_H \sim 0.8$ .

When simulated Monte Carlo top to lepton+jets events are subjected to a conventional 2C fit, the Tevatron collider experiments obtain a mass lineshape which has a  $\approx 15\%$  rms width, and they observe a flattening of the response function  $\partial\langle m_t \rangle / \partial m_{\text{gen}} \approx 0.6$ , where  $\langle m_t \rangle$  is the mean fit mass and  $m_{\text{gen}}$  is the generated top mass. (This flattening arises from the effects of gluon radiation and jet misassignment.) If background is neglected, from these elementary considerations one expects a random error in the fit mass of roughly  $15\%/0.6\sqrt{N} = 25\%/\sqrt{N}$  for an  $N$  event signal.

At present we quote a  $10\%$  random error on  $m_t$  based on fitting 24 "loose cut" candidates divided equally between signal and background. This gives  $35\%/\sqrt{N}$ ; the inflation arises mainly from the effects of background in the fit. Even this conservative estimate results in a random error of only  $1.3\%$  with the full Run II top statistics. Clearly, then, the Run II top mass precision will be dominated by systematic errors. At present in  $D\bar{O}$ , foremost among those is the energy scale error of  $10\%$ . We have already exhibited a  $2.3\sigma$  mass peak in the  $m_t - m_W$  plane; in Run II we plan to use a similar  $W$  mass peak to fix the hadronic calorimeter energy scale for top mass reconstruction. We expect less than a  $2\%$  statistical error on this method of calibration.

Among the residual systematic errors, perhaps the least reducible is the difference between the actual pattern of gluon radiation and that predicted by the available parton shower Monte Carlo calculations. At present we observe  $>2\%$  differences in the means of distributions of fit mass for HERWIG and ISAJET top samples; the peaks of these distributions, to which fits can be especially sensitive, exhibit still larger shifts. Uncertainties

associated with radiative corrections will be more severe at the LHC; even after experiments begin collecting data there, the facility of choice for precise top mass measurement may continue to be the Tevatron.

DØ possesses a unique advantage for controlling errors due to radiative corrections. This is its fine calorimeter granularity, surpassing that of any existing or planned hadron collider detector. We plan to use this detailed calorimeter information to measure the initial and final state radiation and to recombine the latter. Our techniques in this area are still primitive. However, we are already able to demonstrate clustering algorithms able to detect, on average, >2 extra gluons per top event, and mass fitting algorithms able to identify and recombine these gluon jets. Relative to the conventional practice of fitting only the four leading jets, these algorithms improve the mass resolution and, more important, reduce the systematic uncertainties associated with these radiative corrections. Our detailed GEANT simulation of the calorimeter will also contribute to reducing these uncertainties, particularly as we gain more experience in benchmarking the simulations against real data.

### 3.2.3.3 Top Quark Decay Properties

With approximately 1000 background-subtracted  $t\bar{t}$  candidates, it will be possible to test the standard model predictions of the decay properties of the top. The electronic and muonic branching ratios will be measured to 15% each, providing a key check on the Standard Model. The rate of double *vs.* single *b* lifetime tags should determine the  $t \rightarrow b$  branching fraction to 5%, and thus the CKM matrix element  $V_{tb}$  to less than 3%. By fitting the angular distribution of the lepton from decay of  $W$  from top, it should be possible to measure the  $\approx 70\%$  branching ratio of top to longitudinally polarized  $W_L$  with a 3-5% error, thus limiting the  $V + A$  coupling at the  $W$  vertex.

### 3.2.4 Single top production

Single  $t$  production has been studied using a fast simulation which includes parameterized DØ detector resolutions and assumes a  $b$ -tagging efficiency of 50% per jet and a lepton reconstruction efficiency of 75%. (These are the current Run I efficiencies; the improvements for Run II have not been taken into account here). The expected dominant process for single top quark production in  $p\bar{p}$  collisions is via  $W$   $t$ -channel production. *e.g.*  $u\bar{b} \rightarrow d\bar{t}$  with the  $\bar{b}$  supplied by the antiproton sea. For a 200 GeV top quark, this process accounts for three quarters of the 1.7 pb single top cross section, yielding 3400 events in  $2 \text{ fb}^{-1}$  at  $\sqrt{s}=1.8 \text{ GeV}$ . Of these,  $\approx 750$  are tagged by  $e$  or  $\mu$  semileptonic decay. After efficiencies and cuts, about 400 events are expected in a 100 GeV band centered at the top mass above a  $\approx 300$  event background. The dominant background processes are  $p\bar{p} \rightarrow Wb\bar{b}$  and  $p\bar{p} \rightarrow t\bar{t}$ . The distribution of reconstructed top mass for signal and backgrounds, after cuts, is shown in Fig. 12.

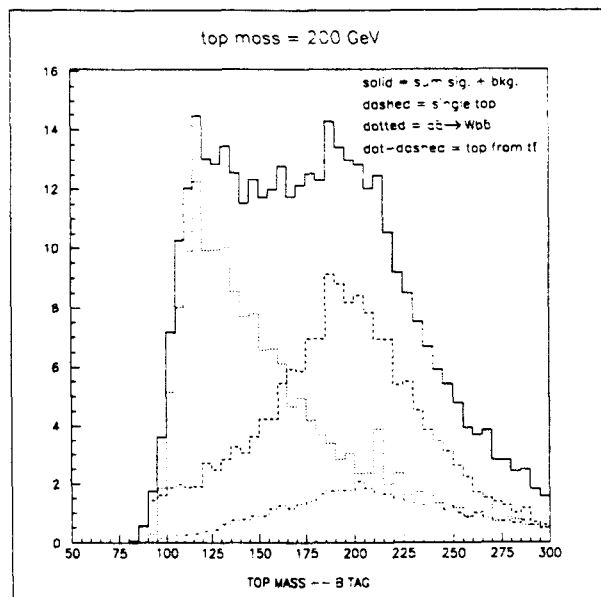


**Figure 12.** Distribution of reconstructed top mass for single top signal ( $m_t = 200 \text{ GeV}$ ) and  $t\bar{t}$  and  $Wb\bar{b}$  backgrounds, after cuts, for an integrated luminosity of  $1 \text{ fb}^{-1}$ .

With  $1 \text{ fb}^{-1}$  of data it will be possible to measure the single top cross section with a precision of about 10%. The full width of the top is not measurable in the  $t\bar{t}$  state, but can be extracted directly (within theoretical uncertainties) from the single top cross section; a  $\approx 20\%$  top width measurement should be feasible. Single top events will also provide an interesting cross-check of the top mass, since the multi-jet combinatoric problems are much less severe here.

### 3.2.5 Search for the Charged Higgs Boson in Top Decays

The present limit on the mass of the charged Higgs boson predicted by minimal supersymmetry ( $m_{H^\pm} > 45 \text{ GeV}/c^2$ ) is from LEP measurements. By the time the DØ Upgrade run is underway, we expect this limit to increase to  $\gtrsim 100 \text{ GeV}/c^2$ , the exact value depending on the maximum energy reached by LEP 200. Assuming that the charged Higgs is lighter than the top quark, one can search for top quark decays into a charged Higgs and a  $b$  quark in addition to its usual decay into  $W$  and a  $b$  quark. The charged Higgs will have two predominant decay modes, into  $c\bar{s}$  and into  $\tau\nu$ , the relative branching ratios depending on the  $\tan\beta$  parameter of the minimal supersymmetric model. The Higgs decay will not contribute to the DØ dilepton top search channels of  $ee$ ,  $e\mu$  and  $\mu\mu$  except by the secondary decay of the  $\tau$ , which we neglect in the present calculation. The lepton + jets channels  $e + jets$  and  $\mu + jets$  will have contributions from both  $W$  decays and from charged Higgs decays.

There are several ways of searching for the charged Higgs in top quark decays.

- Searching for an apparent violation of lepton universality in top decays. An excess of  $\tau$  decays compared with  $e$  and  $\mu$  modes would signal the presence of a charged

Higgs decay mode. The  $D\mathcal{O}$  upgrade, with its excellent tracking and finely segmented calorimetry is very well suited to precision  $\tau$  studies.

- Counting the overall event rate and comparing it to the standard model QCD top production cross section. For an increase in the branching ratio  $t \rightarrow H^\pm + b$  (determined by the parameter  $\tan\beta$  in minimal supersymmetry) the total number observed events in  $e$  and  $\mu$  channels falls. Comparing with the standard model top production cross sections enables a limit to be placed in the  $m_{H^\pm}-\tan\beta$  plane.
- Since the charged Higgs contributes only to lepton + jets channels and not the dilepton channels, we can look for departures in the relative event rates in these two channels. This method does not assume the standard model QCD top quark production cross section.
- Look for effective mass peaks in the dijet system removed from the  $W$  peak. This method can in principle measure the mass of the charged Higgs, should it contribute significantly to top quark decays. However, as a search method, it is limited by the resolutions obtainable in the jet-jet effective mass.

### 3.2.6 Discovery of New Physics in the $t\bar{t}$ Channel

The top quark's large mass makes it unique among the elementary fermions in having a coupling to the SM Higgs of order unity; it is the only fermion not to be approximately massless on the scale of electroweak symmetry breaking. It therefore offers a dramatic example of broken flavor symmetry and a window into possible physics beyond the standard model — for example, to scenarios where electroweak symmetry is dynamically broken at a scale of order the top quark mass. Examples of such models are multiscale technicolor<sup>[9]</sup>, color octet vector mesons  $V_8$  associated with  $t\bar{t}$  condensation,<sup>[10]</sup> and electroweak isoscalar quarks  $t_s$ .<sup>[11]</sup> The cross section,  $t\bar{t}$  invariant mass, and centre-of-mass angular distributions may all be used to search for new physics.

The  $t\bar{t}$  cross section is enhanced by most of these models. For example, in multiscale technicolor, a color-octet technipion  $\eta_T$  which occurs with mass 400–500 GeV can easily double the  $t\bar{t}$  rate. If the  $\eta_T \rightarrow t\bar{t}$  partial width is not too large, (e.g. the coupling  $C_t \sim \frac{1}{3}$ ) then a peak at the  $\eta_T$  mass will easily be seen in the  $t\bar{t}$  invariant mass distribution (with a natural FWHM of about 20 GeV) with  $1 fb^{-1}$  of integrated luminosity. If  $C_t \sim 1$  then the  $\eta_T \rightarrow t\bar{t}$  peak is much broader, and the mass peak is too wide for direct observation; the enhancement of the  $t\bar{t}$  cross section will still be obvious.

Subsystem invariant masses may also be sensitive to new physics. For example, a color-octet technirho  $\rho_T$  may be produced and decay via  $\rho_T \rightarrow W\pi_T^\pm$ , with  $\pi_T^\pm \rightarrow t\bar{b} \rightarrow Wb\bar{b}$ . the same final state as in  $t\bar{t}$  production. Searches for processes such as this will be possible with  $1 fb^{-1}$  of data.

Another sensitive distribution is the centre-of-mass angle of the top quarks. The Tevatron has a distinct advantage in this case, as the annihilating quark and antiquark directions are strongly correlated with those of the proton and antiproton. Measurements of forward-backward asymmetry ( $A_{FB}$ ) are therefore much cleaner than at the LHC, where  $t\bar{t}$  production is dominated by  $gg$  fusion. It is found<sup>[12]</sup> that  $1 fb^{-1}$  of data is sufficient to

distinguish. at the  $5\sigma$  (statistical) level, the  $A_{FB}$  arising from  $V_8$ -enhanced top production from the standard QCD mechanisms.

### 3.3 Electroweak Physics and Precision Tests of the Standard Model

Because of its success in describing low energy phenomenology and its relative economy in the number of fundamental fields, the  $SU(3)_c \times SU(2)_L \times U(1)$  theory of strong and electroweak interactions, based on the principle of non-abelian gauge invariance, has become the Standard Model.  $SU(3)_c$  embodies the current theory of the strong interactions, Quantum Chromodynamics, and is deemed to be an unbroken symmetry of nature. The  $SU(2)_L \times U(1)$  sector is the basis of the Standard Electroweak Model and is spontaneously broken at a mass scale  $v = (\sqrt{2}G_\mu)^{-1/2} = 246$  GeV into  $U(1)_Q$ , the abelian gauge group of electromagnetism.

The Standard Model has been very successful phenomenologically. It has provided the theoretical framework for the description of a very rich phenomenology spanning a wide range of energies, from the atomic scale up to  $m_Z$ . It is being tested at the level of a few tenths of a percent, both at very low energies and at high energies. The aim of these studies is to test the theory at the level of its quantum corrections and to search for deviations that may signal the presence of "new physics".

#### 3.3.1 $W$ boson mass

A prime measurement that is sensitive to quantum corrections is the precision measurement of the  $W$ -mass, which provides a critical test of the Standard Model. The current preliminary  $D\bar{O}$  measurement of the  $W$ -mass, based on central electrons only, presented at the 1993 Tsukuba workshop on  $\bar{p}$ - $p$  collider physics, is

$$\begin{aligned} m_W^e &= 79.86 \pm 0.16 \pm 0.16 \pm 0.26 \text{ GeV} \\ &= 79.86 \pm 0.35 \text{ GeV} \end{aligned}$$

where the errors are statistical, systematic and energy scale systematic, respectively. The current world average  $W$ -mass, using preliminary values for both the CDF and  $D\bar{O}$   $W$ -boson mass, is

$$m_W = (80.23 \pm 0.18) \text{ GeV (World Av., 1994)}$$

where the combination assumes a common error of  $\pm 100$  MeV. It is anticipated that the error on the final Run 1a  $W$ -mass measurement will decrease significantly.

Table 3 lists the dominant uncertainties on the  $W$ -mass measurement. The error due to the uncertainties in the absolute energy scale, in the relative response of the hadronic to the electromagnetic calorimeter, in the resolution and the uncertainty in the neutrino momentum scale are all dominated by the statistical error on the number of  $Z$ -events. It is therefore expected that the error on the  $W$ -mass will approximately scale as  $1/\sqrt{N}$  for integrated luminosities reaching  $2 \text{ fb}^{-1}$ . Some systematic errors are quasi-theoretical in nature and are associated with the details of the production process. In the case of the  $W$   $p_T$  spectrum, the  $Z^0$  spectrum is expected to provide appropriate checks. The structure

function effects are controlled in part through the measurement of the  $W$  asymmetry. It is expected that with the upgraded DØ detector with two  $W$ -mass measurements, one from the electron channel and one from the muon channel, a precision of about 50 MeV can be obtained with an integrated luminosity of  $2 \text{ fb}^{-1}$ .

Source of Uncertainty	MeV/c <sup>2</sup>
Statistical	160
Absolute energy scale	260
Resolution and neutrino $p_T$ scale	100
Efficiencies	25
Energy underlying electron	50
Hadronic to EM scale	80
QCD background	30
Theoretical model uncertainty	85
Fitting Error	30
<b>Total</b>	<b>350</b>

**Table 3.** Systematic uncertainties on the  $W$  mass measurement(DØ Preliminary)

At high luminosities and large number of interactions per bunch crossing, alternative methods for determining the  $W$ -mass may be pursued. Given enough statistics a determination of the  $W$ -mass using the transverse lepton momentum spectrum may have less systematic uncertainties associated with the measurement than the determination using the transverse mass spectrum. A direct measurement of the ratio of the  $W$ - and  $Z$ -mass may also be free of more systematic uncertainties.

The value of  $m_W$  and  $m_t$  can also be inferred from the precision electroweak measurements. The  $1\sigma$  and  $2\sigma$   $m_t - m_W$  contours from a Standard Model global fit to the measured electroweak parameters from  $e^+e^-$ -collisions is shown in Fig. 13. The mass  $m_H$  of the Higgs boson is unconstrained in these fits. The shaded bands correspond to lines of constant  $m_H$ , with the width of the bands being due mainly to the uncertainty in  $\alpha(m_Z)$ . It is clear that a precision measurement of  $m_W$  and  $m_t$  would constitute a significant test of the Standard Model. We illustrate this with a hypothetical Run II measurement with errors of 50 MeV and 5 GeV respectively.

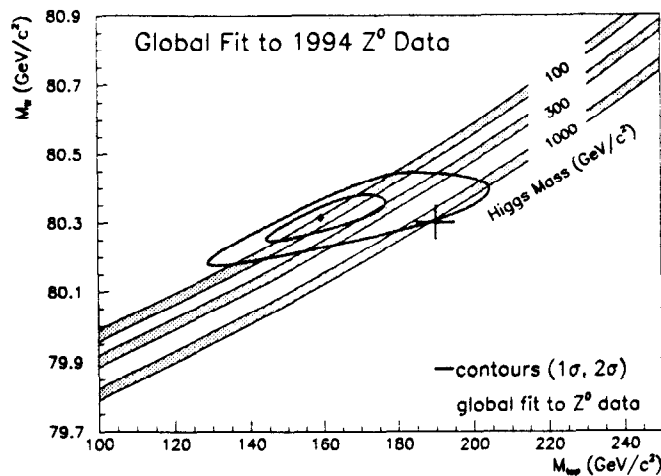


**Figure 13.**  $m_t - m_W$  contours from a global Standard Model fit all  $e^+e^-$  and  $\nu N$  data. the global fit,  $m_H$  is a free parameter; it ranges from to 180 GeV on the 1- $\sigma$  contour. cross-hatched bands correspond to the indicated masses; the widths of the bands are due primarily to the error in  $\alpha(m_Z)$ . A hypothetical Run II measurement is shown.

### 3.3.2 $W$ Boson Decay Properties

The couplings of the  $W$  to other particles are additional parameters which are predicted by the Standard Model and which can be determined from the measured partial widths of the  $W$  to specific final states. Deviations from the Standard Model predictions could signal new decay modes (e.g.,  $W \rightarrow t\bar{b}$  for a light top) or loop corrections involving new particles or new couplings. Both  $\Gamma_W$  and  $B(W \rightarrow l\nu) = \Gamma(W \rightarrow l\nu)/\Gamma_W$  have been measured in hadron collider experiments.

An indirect measurement of  $B(W \rightarrow l\nu)$  can be carried out by using the measured event ratio  $R = \sigma B(W \rightarrow l\nu)/\sigma B(Z \rightarrow l^+l^-)$ , multiplied by the theoretical production cross-section ratio  $\sigma(p\bar{p} \rightarrow Z)/\sigma(p\bar{p} \rightarrow W)$  and the LEP measurement of the branching ratio  $B(Z \rightarrow l^+l^-)$ . The published world average<sup>[13]</sup> for the leptonic branching ratio is  $B(W \rightarrow l\nu) = 0.107 \pm 0.005$ , to be compared with the Standard Model expectation<sup>[14]</sup> of  $0.1084 \pm 0.0002$ . The agreement between the measurement and theory can be used to exclude a light top ( $m_t < 62$  GeV) in a way which is independent of any assumptions about top decay modes. In the future, the error in  $B(W \rightarrow l\nu)$  is likely to be limited at about the 1% level by the theoretical uncertainty in the production cross-section ratios.

The width of the  $W$ -boson can also be measured directly based on the measured shape, and especially the high-mass tail, of the transverse mass distribution of  $W \rightarrow e\nu$  events.<sup>[15]</sup> In the region far above  $m_W$  the effects of the largely gaussian resolution of the detector die off and the distribution is determined by the Breit-Wigner line shape of the  $W$ -decay. After  $1 \text{ fb}^{-1}$  of data, an error in  $\Gamma_W$  of about 50 MeV is expected. This precision approaches the level of radiative corrections to the width.

Furthermore, the direct measurement of the  $W$  width may be combined with the leptonic branching ratio measurement to provide a measurement of  $\Gamma(W \rightarrow l\nu)$ . This leptonic partial width is predicted to be  $\Gamma(W \rightarrow l\nu) = g^2 m_W / 48\pi$ , and thus its measurement may

be used to determine  $g$ . In conjunction with the measured leptonic branching ratio, this would give a measurement of  $\Gamma(W \rightarrow l\nu)$  at the 1.8% level, and consequently an error on the  $W$ - $l\nu$  coupling  $g$  of 0.9%. The extraction of  $g$  from  $\Gamma(W \rightarrow l\nu)$  is more reliable because it is not sensitive to QCD corrections that are present in the  $\Gamma(W \rightarrow q\bar{q})$  widths.

### 3.3.3 $W$ and $Z$ Asymmetry Measurements

Using the solenoidal magnetic field to measure the sign of the charge of electrons and positrons, the upgraded DØ detector will be able to study the forward-backward asymmetry ( $A_{FB}$ ) in  $p\bar{p} \rightarrow \ell^+\ell^-$  events. Since the asymmetry arises from the parton level process  $q\bar{q} \rightarrow \ell^+\ell^-$  it depends on the vector and axial vector couplings of the quarks and leptons to the  $Z$  and is therefore sensitive to  $\sin^2\theta_W$ . This measurement of  $\sin^2\theta_W$  is for light quarks only. The current error on the equivalent quantity from LEP is 0.0016, which is limited by understanding the effects of fragmentation on  $A_{FB}$ . With a data set of  $1 \text{ fb}^{-1}$ , DØ will be able to measure  $\sin^2\theta_W$  with an error of 0.001 free of fragmentation effects.

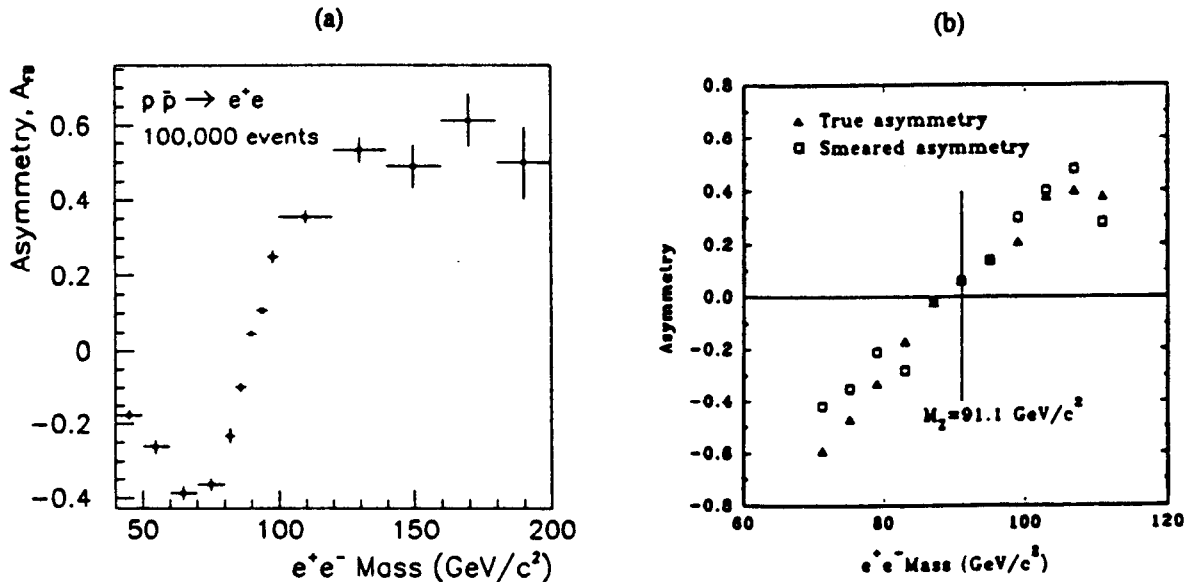


**Figure 14.** Forward-backward asymmetry  $A_{FB}$  as a function of  $e^+e^-$  invariant mass in  $p\bar{p} \rightarrow e^+e^-$  events. (a) statistical errors for  $1 \text{ fb}^{-1}$  in an ideal detector; (b) effect of DØ calorimeter resolution.

Figure 14(a) shows the variation of  $A_{FB}$  with the  $e^+e^-$  invariant mass in  $p\bar{p} \rightarrow e^+e^-$  events at  $\sqrt{s} = 1.8 \text{ TeV}$ . The error bars indicate the statistical errors for 100,000 events, corresponding to an integrated luminosity of about  $2 \text{ fb}^{-1}$ . From this simulation we estimate the statistical error on  $\sin^2\theta_W$  to be 0.001 for  $1 \text{ fb}^{-1}$  and 0.00035 for  $10 \text{ fb}^{-1}$ .

A preliminary study of the systematic errors indicates that most sources of error are small compared with the statistical error for a  $1 \text{ fb}^{-1}$  data set. The effect of the electromagnetic calorimeter energy resolution is rather small, as shown in Fig. 14(b). The main contribution to the systematic error is from the uncertainty in the parton distribution functions – since the vector and axial vector couplings of  $u$  and  $d$  quarks to the  $Z$  are

different, the measured asymmetry depends on the ratio of  $u$  to  $d$  quarks in the proton. The measurement is primarily a test of our understanding of the couplings of the different quarks within the Standard Model. Alternatively, one may assume the SM couplings and use the world average value of  $\sin^2\theta_W$  (with its smaller errors) to constrain the parton distributions of the proton at high  $Q^2$ . Studies are in progress to quantify this.

### 3.3.4 Anomalous Vector Boson Couplings

One of the most direct consequences of the  $SU(2)_L \times U(1)_Y$  gauge symmetry is the non-abelian self-couplings of the  $W$ ,  $Z$  and photon. A direct measurement of these vector boson couplings is possible through the study of pair production processes like  $q\bar{q} \rightarrow W^+W^-$ ,  $W\gamma$ ,  $Z\gamma$ ,  $WZ$ . The first and major goal of such experiments will be a confirmation of the Standard Model predictions. A precise and direct measurement of the trilinear and quartic couplings of the electroweak vector bosons and the demonstration that they agree with the Standard Model would beautifully corroborate spontaneously broken, non-abelian gauge theories as the basic theoretical structure describing the fundamental interactions of nature. At the same time, such measurements may be used to probe for new physics. It is possible that signals for physics beyond the Standard Model will appear in this sector through the observation of anomalous trilinear (or quartic) gauge-boson vertices.

Because of the subtle cancellations between the different processes for di-boson production in the Standard Model, any deviation of the couplings from their standard model values will result in an increase in cross section. Furthermore, differential distributions will be significantly modified. For  $W\gamma$ ,  $Z\gamma$  production, for example, the photon  $p_T$  spectrum exhibits a significant increase in event rate for high  $p_T$  photons. By comparing the shape of the measured and predicted  $p_T$  distribution limits on anomalous  $WWV$  and  $Z\gamma V$  couplings can be obtained. Figure 15 shows the limits on the anomalous  $WW\gamma$  and  $ZZ\gamma$ -couplings derived from the Run Ia data.

The substantial increase in integrated luminosity delivered for Run II will make it possible to test the  $WWV$  and  $Z\gamma V$  vertices with much greater precision than in current experiments. In Fig. 16 the 95% CL limits on anomalous  $WW\gamma$  and  $ZZ\gamma$  couplings are shown expected from  $W\gamma$  and  $Z\gamma$  production at the Tevatron ( $\sqrt{s} = 2$  TeV) for  $1 \text{ fb}^{-1}$  and  $10 \text{ fb}^{-1}$ . It can be seen that the current limits on anomalous gauge boson couplings can be improved by about a factor 5 – 15 (10 – 100) in  $W\gamma$  ( $Z\gamma$ ) production in the Main Injector era. An additional factor 10 in integrated luminosity leads to roughly a factor 2 improvement in the sensitivities which can be achieved. It should be noted that the limits quoted here are based on electron decays only. The limit contours shown can be improved by about 20 – 40% if  $W \rightarrow \mu\nu$  and  $Z \rightarrow \mu^+\mu^-$  decays are included in the analysis.

In addition to  $W\gamma$  and  $Z\gamma$ -production,  $W^+W^-$ ,  $W^\pm Z \rightarrow \ell\nu jj$  and  $WZ \rightarrow \ell^+\ell^-jj$ ,  $\ell = e, \mu$  production can be studied non-standard  $WWV$  couplings. The sensitivity of these processes to anomalous couplings is similar to the sensitivity in  $W\gamma$  and  $Z\gamma$ -production.

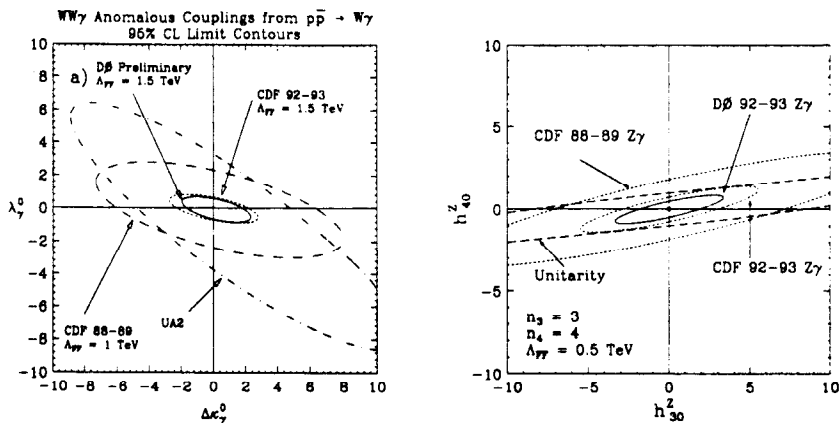


Figure 15. 95% CL limits on anomalous  $WW\gamma$  and  $ZZ\gamma$ -couplings derived from  $D\bar{O}$  Run Ia data.

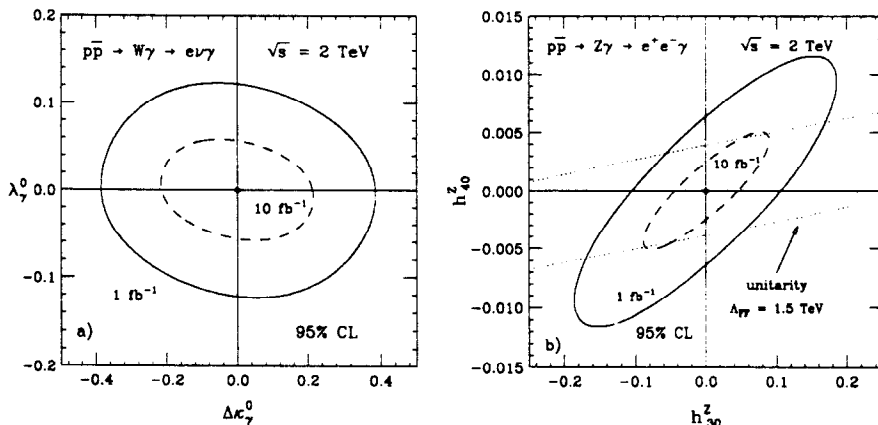


Figure 16. 95% CL limits on anomalous  $WW\gamma$  and  $ZZ\gamma$ -couplings obtainable with  $1 \text{ fb}^{-1}$  and  $10 \text{ fb}^{-1}$  of data.

### 3.4 QCD

#### 3.4.1 Introduction

The data gathered at the Tevatron in Runs Ia and Ib have already resulted in many new and rigorous tests of QCD. Several years will be required to exploit fully the data taken with the current  $D\bar{O}$  detector at present luminosities. In particular, measuring differential cross-sections for jet, photon, and intermediate vector boson production with respect to increased numbers of event variables (momenta, pseudorapidities, etc.) will explore new regions of phase space particularly sensitive to parton distribution functions and higher order QCD calculations. These multi-dimensional cross-sections will also guide the way for establishing non-perturbative descriptions of partonic interactions, which are important at the edges of phase space. The large total luminosities expected for Run II will also encourage searches for new phenomena such as quark compositeness and excited quarks, rare diffractive processes, and vacuum polarization, and will provide accurate tests of all aspects of QCD because the theoretically and experimentally well described  $W/Z$ +jet samples will have statistical significance rivaling that of the present dijet samples. As

QCD moves into this era of precision, rather than qualitative, tests, confrontation between theory and experiment at higher integrated luminosities and with an upgraded detector will be of great importance. The addition of a central magnetic field will also allow the study of more exclusive final states such as  $W$ +charm and  $\gamma$ +charm. The current QCD program with the  $D\bar{O}$  detector is rich and imaginative and we are confident that this will continue with the upgraded detector. We have already presented analyses in areas of physics previously unexplored at the Tevatron: rapidity gaps, correlations between jets with large rapidity intervals, the measurement of  $\alpha_S$ , and energy flow around the jets, as well as the development of a new jet finding algorithm.

### 3.4.2 Parton Distributions

Until recently, cross-sections measured at the Tevatron have been used to verify the accuracy of current parton distribution parametrizations. This is one of the best tests of QCD because it requires the perturbative calculation of the QCD hard parton cross-sections *and* the QCD evolution equations to extrapolate the parton distributions from low energy fixed target experiments to the Collider energy scales. This is a rigorous test of factorization since the energy scales tested differ by more than an order of magnitude. Measurement of the total inclusive jet or photon cross-sections are examples of such tests.

Until now, however, the Tevatron results (except for the  $W$ -asymmetry measurement) have not been used to fix the parton distributions. This will change in the next few years as studies focus on measuring differential cross sections with respect to an increased number of variables for jets,  $\gamma$ 's, and  $W/Z$  final states with larger statistics. For example, consider the triple differential cross-section  $d^3\sigma/dp_{T1}d\eta_1d\eta_2$  where  $p_{T1}$  and  $\eta_1$  are the leading jet transverse momentum and  $\eta_2$  the rapidity of the second leading jet.<sup>[16]</sup> At small leading momentum and rapidity,  $p_{T1} = 50$  GeV and  $\eta_1 = 0$ , and large values of rapidity for the second jet,  $\eta_2 = 2.5$ , the cross-section is sensitive to the product of parton momentum fractions at extreme values of  $x$  (between 0.003 and 0.7). As a second example of differential cross-sections, the  $\gamma$  inclusive cross-section  $d^2\sigma/dp_t^\gamma d\eta$  and the  $\gamma$ +jet inclusive cross section at large rapidities are sensitive to the gluon content of the proton at  $x = 0.001$ .

Looking ahead further one can anticipate the measurement of specific parton flavors in the proton, by selecting certain exclusive final states. This is very difficult with the current  $D\bar{O}$  detector, but is made possible by the upgraded tracking system. An example here is the final state  $W$  + charm, which directly probes the strange quark distribution. Another example would be  $\gamma$  + charm or any other process where the final state quark could be tagged. Charm identification will be possible both through reconstruction of the exclusive  $D$  decay modes, and through tagging soft muons from the charm decay.

### 3.4.3 Next-to-Leading Order and Beyond

The differential jet,  $\gamma$ ,  $W$  and  $Z$  cross-sections just discussed also provide precise tests of QCD calculations at order  $\alpha_s^3$ (NLO). These calculations for differential jet production are now available.<sup>[17,18]</sup> For large jet rapidities, leading order calculations seriously underestimate the cross section. NLO calculations compensate for this shortfall but not completely. Most likely even higher order calculations are necessary and these are currently being worked on. The examination of rare high  $p_T$  and very forward jets, possible only with high luminosity, will be a further revealing test of NLO calculations. The large pseudorapidity coverage of the DØ calorimeter ( $|\eta| \lesssim 4$ ) is ideally suited to these measurements.

Currently, precision studies of QCD with jets are limited in DØ because the jet energy scale has large systematic errors. This error will be greatly reduced in the upgraded detector, because tracking in a magnetic field will allow a calibration of the hadron energy scale *in situ* for the first time.

At very low transverse momentum or at the edge of accessible phase space, one expects non-perturbative effects, like primordial parton  $k_T$ , to play a role. It has been suggested that such effects can explain the discrepancies in direct photon cross sections at different center of mass energies. A universal formulation of such non-perturbative phenomena is being attempted now,<sup>[19]</sup> and its predictions can be tested in other processes at the Collider. To test the transition from perturbative to non-perturbative calculations, both large acceptance and high luminosities are required. The  $W$  and  $Z$   $p_T$  spectra test a similar transition since the low  $p_T$  portion of the spectrum is calculated by resummation techniques, with the above mentioned non-perturbative contributions, and matched to the high  $p_T$  perturbative part of the spectrum.

NLO calculations for di-photon and intermediate vector boson production are available but have not been precisely tested.<sup>[20,21]</sup> The high statistics samples required for these NLO tests must wait for higher luminosities or, equivalently, higher energies.

### 3.4.4 Drell-Yan ( $W/Z$ ) Production

Drell-Yan pairs provide a clean probe of QCD processes. The colorless muons or electrons are free of final-state interactions and can be accurately identified without any of the ambiguities of jet identification and measurement. Typically, cross sections are small, and as a result Drell-Yan production has not been used to its full potential. However, the special cases of  $Z$  and  $W$  production have recently been used to test perturbative, resummed, or parton shower based predictions of QCD. Two examples include the determination of  $\alpha_s$  from  $W$ +jets and the comparison of  $Z$  and  $W$   $p_T$  distributions with resummed predictions.

$Z$  production alone can be considered an outstanding QCD test laboratory. Because the final state  $Z$  can be reconstructed very accurately and without background, the measurement of  $p_T$ ,  $p_L$ , rapidity dependence, and energy flow around the  $Z$  can be made in an unambiguous and unique way. This kind of detailed study of QCD is just starting to become feasible with currently available luminosities. With higher luminosities, it can reach the statistical precision of jet cross sections but without any of the hindrance from systematics. To reach this statistical precision one would need a sample of roughly  $10^5$   $Z$ 's, which corresponds to about  $1fb^{-1}$  if one uses the  $Z \rightarrow e^+e^-$  and  $Z \rightarrow \mu^+\mu^-$  decays.

In fact, the entire menu of differential jet and photon cross-sections can be replaced with differential  $Z + \text{jet}$  final state cross-sections. This will truly move QCD into the realm of precision physics. An obvious measurement here would be the determination of  $\alpha_S$  from the ratio of  $Z + n\text{jet}/Z + (n - 1)\text{jet}$ . This would be similar to what has already been done with  $W$ 's, but much more precisely determined experimentally.

The special case of  $Z$  production can be generalized by introducing the Drell-Yan ( $\gamma^* \rightarrow l^+l^-$ ) pair mass as a parameter. In particular, measurement of the Drell-Yan pair  $p_T$  distribution as a function of mass provides a test of resummation techniques. The more interesting measurement though would again be the determination of the strong coupling constant. One employs the same technique as for  $Z$ 's, but as a function of the lepton pair invariant mass. This results in a measurement of  $\alpha_S$  as a function of  $Q^2$  scale, and tests both the running of  $\alpha_S$  and its absolute value in one experiment. With sufficient statistics the angular distribution of the final state leptons may also analyze the polarization state of the vacuum,<sup>[22]</sup> a possibility that has, as yet, not been investigated at the collider. Including both electron and muon final states, one expects about 60K events in the region  $20 < m_{\gamma^*} < 30$  GeV.

### 3.4.5 Jet Algorithms and Studies of Jet Structure

$D\bar{O}$  has developed a new jet-finding algorithm based on the successive-combination techniques commonly used in  $e^+e^-$  physics. The same algorithm may be used to find clusters of energy within jets. With large statistics, we hope to be able to statistically separate quark and gluon jets using this approach and thus refine our study of the QCD subprocesses. It should also be possible to measure both  $\alpha_S$  and observe its running from the dependence of the observed number of jets on the combination scale used in the algorithm.

### 3.4.6 Rapidity Gaps, Diffractive Scattering and the Pomeron

Dijet production at large rapidity differences,  $\Delta\eta \gtrsim 4$ , with little or no activity between the jets (rapidity gaps) may signal the presence of the exchange of a colorless object.<sup>[23]</sup> Such events have been observed by  $D\bar{O}$  in its current run and we want to examine this phenomenon further in the future. Is the exchanged object the Pomeron and is it the same object observed in diffractive scattering? By studying diffractively produced events at the Tevatron the partonic content of the Pomeron may be measured. Is it the same as measured at HERA and at UA8? These questions can partially be answered with events with rapidity gap signatures, but ultimately may require the measurement of the diffractively scattered (anti-)proton.  $D\bar{O}$  has begun to investigate the potential for pursuing rapidity gap and diffractive physics in Run II.

## 3.5 B-Physics

### 3.5.1 Introduction

The upgraded  $D\bar{O}$  detector will address a variety of  $B$  physics, ranging from QCD tests involving production dynamics through the mass spectrum of the  $B_c$  system, rare decay modes,  $B_s$  mixing and CP violation. Apart from the last, the Tevatron is the only (or the pre-eminent) facility where these fundamental issues may be addressed. The  $D\bar{O}$  detector's

full  $\eta$  coverage is particularly well matched to measurements of  $B$ -mesons — beauty is produced uniformly in pseudorapidity. Mesons produced centrally are typically soft, with  $\gamma < 3$ , putting a premium on soft lepton triggers and minimal multiple scattering. The low boost for centrally produced  $B$ 's implies decay fragments which are distributed in  $\eta$ . In addition much of the most interesting physics, such as mixing and CP violation, requires that both partners in the  $B\bar{B}$  pair be at least partially reconstructed. Physics which requires either full reconstruction of the final state or tagging of the partner  $B$  will be quite sensitive to the coverage of the tracking system. The strengths of the upgraded  $D\phi$  detector for  $B$ -physics, then, are its full calorimetric and muon coverage, its dedicated forward tracking systems, and its ability to trigger on low- $p_T$  leptons over the whole pseudorapidity range  $|\eta| \leq 3$ .

Although  $B$  mesons are produced copiously (about 2000  $B\bar{B}$  pairs per second at  $\mathcal{L} = 10^{32} \text{ cm}^{-2}\text{s}^{-1}$ ) studies of mixing and CP violation are still likely to be limited by statistics. Final states must be fully reconstructed and the initial state must be tagged. CP violating decay modes are typically at the  $10^{-5}$  level. We will need fully reconstructed decay chains with typical branching ratios of  $\sim 10^{-4}$  to obtain sufficient resolution for  $B$ , mixing measurements. The experimental challenge is to trigger on, collect, and reconstruct these events.

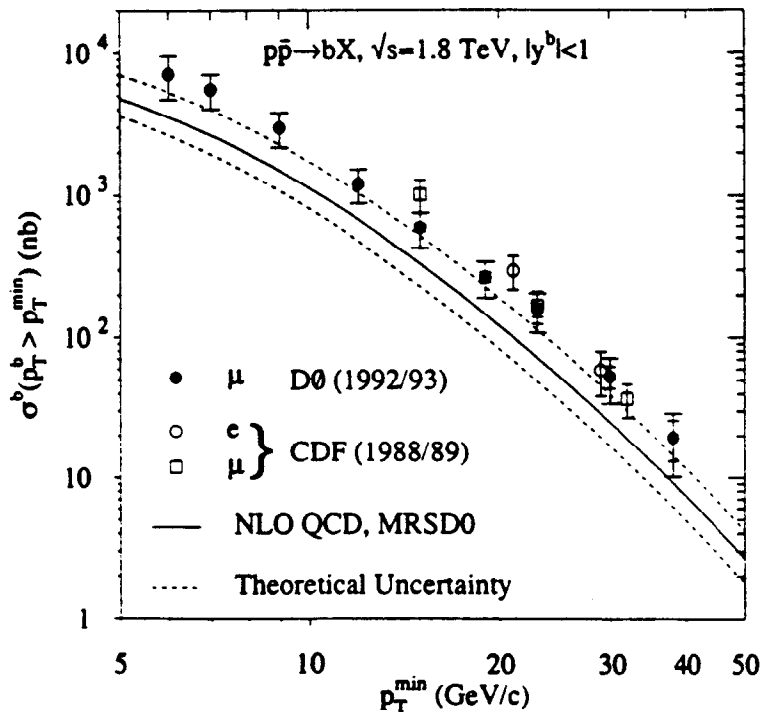


**Figure 17.** Inclusive  $p\bar{p} \rightarrow b$  cross section as measured by  $D\phi$  in Run Ia.

$D\phi$  has had an active  $B$  physics program in Run I with an emphasis on the detector's strengths in muon detection and calorimetry.  $D\phi$  has concentrated on studies of hadroproduction of  $b$ 's over an extensive rapidity range (see Fig. 17). Current studies include measurements of inclusive muon and charmonium production (see Fig. 18), the heavy flavor content of jets, and  $B\bar{B}$  correlations.  $B$  production represents a small fraction

(1/1000) of the total cross section. In Run I we have gained a great deal of understanding of how to successfully trigger and reconstruct  $b$ 's. The job is especially difficult in the intermediate to large  $\eta$  range. Our plans represent the results of studying the triggering and reconstruction problems over the full pseudorapidity range.

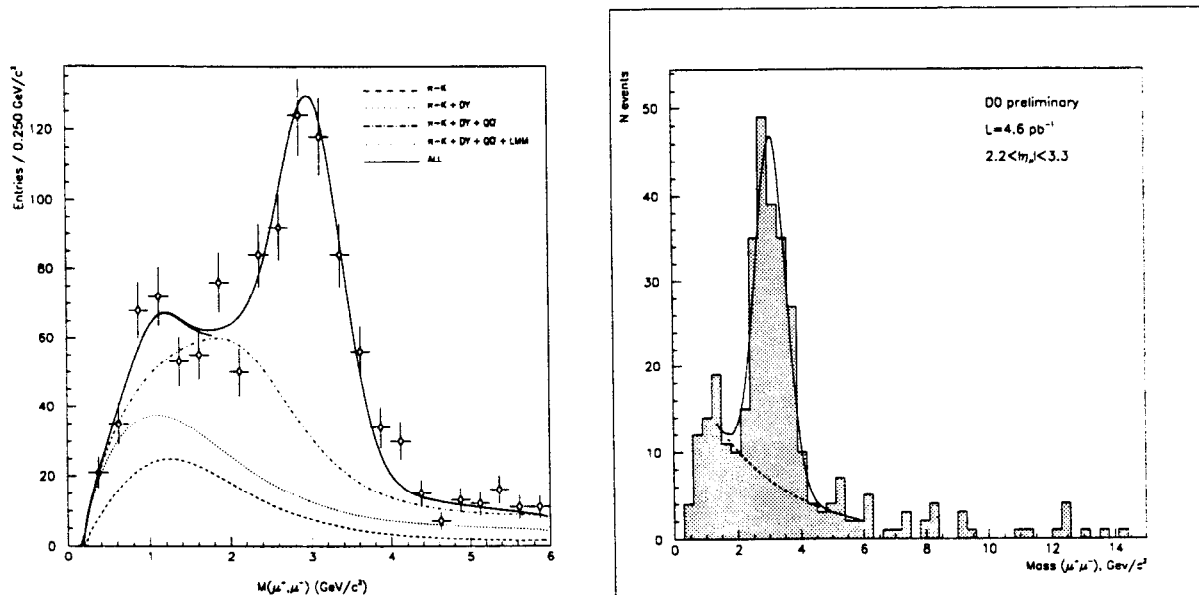


**Figure 18.** Inclusive  $p\bar{p} \rightarrow \mu^+\mu^-$  cross sections as measured by  $D\bar{O}$  in Run Ia, for (a) central and (b) forward muon samples.

The upgrade represents a very significant improvement in  $D\bar{O}$ 's  $B$  physics capabilities. Magnetic tracking allows us to reconstruct the masses of hadronic final states and tag the sign of electrons and hadrons. Our  $J/\psi$  mass resolution will improve by a factor of 10. The Level 1 track processor will improve the overall level of signal/noise by allowing sharp  $p_T$  thresholds for lepton triggers. Combined with the A-layer muon trigger counters, the processor will substantially decrease the muon trigger  $p_T$  threshold, crucial for efficient  $b$  triggering. Signal/noise will also be improved by matching muon system and central tracks at the trigger level. The forward muon pixel counters will allow muon triggering at intermediate  $\eta$ . The silicon vertex detector will allow us to tag decays based on lifetimes, to study mixing, and reduce backgrounds for the whole range of heavy flavor physics. It is a crucial addition for mixing and CP violation studies. In addition the silicon disks provide forward tracking in the detector.  $D\bar{O}$  will be the first experiment to seriously explore heavy quark physics in the forward region.

However, our plans do not represent a complete  $B$ -physics program. To contain costs and meet the laboratory schedule  $D\bar{O}$  has chosen not to upgrade the Level 1 bandwidth beyond 10kHz. We have also chosen to postpone any Level 2 vertex processor. This will limit our  $B$  physics reach in Run II and present some hard choices in our trigger lists.

As examples of Run II  $B$ -physics, we consider two benchmark processes,  $B_s$  mixing and CP violation. The results shown are from recent studies using a fast simulation package.<sup>[24]</sup>

In previous studies we have demonstrated the very high reconstruction efficiency of the upgraded DØ tracking system.

### 3.5.2 Mixing

A measurement of  $B_s$  mixing, along with the measured value for  $B_d$  mixing, will constrain the CKM matrix parameters  $\rho$  and  $\eta$  ( $x_s/x_d \sim 1/((1-\rho)^2 + \eta^2)$ ). The large mass of the top quark suggests a value of  $x_s$  well in excess of ten:  $x_s$  can be measured by taking the difference of mixed and non-mixed events as a function of proper time:  $N(B_s \rightarrow \overline{B}_s) = \frac{1}{2}N_0 e^{-t/\tau}(1 - \cos(x_s t/\tau))$ , where  $N_0$  is the number of  $B_s$  at  $t = 0$  and  $\tau$  is the  $B_s$  lifetime.

We have obtained a qualitative picture of the effects of reconstruction on the lifetime resolution:

- Partial reconstruction of the final state can only provide momentum resolution in excess of  $\sim 20\%$ , which implies a reach of  $x_s \lesssim 10$ .
- In general the statistical loss from full reconstruction of a state like  $B_s \rightarrow D_s \pi$ ,  $D_s \rightarrow \phi \pi$  is more than balanced by increased lifetime resolution for the final state. Our strategy, then, is to aim for fully reconstructed states.
- In the central region the lifetime resolution is dominated by the vertex resolution and is typically  $\sim 5\%$ .
- In the forward region the lifetime resolution is dominated by momentum resolution.
- The momentum resolution can be significantly improved by kinematic constraints on the intermediate states.
- Forward acceptance doubles the  $b$  tagging efficiency.

We expect that with  $1 \text{ fb}^{-1}$  of data, the upgraded detector should be able to measure over 2000  $B_s$  decays with a lifetime resolution of better than 5%. This should allow us to measure values of  $x_s \lesssim 25$ .

### 3.5.3 CP Violation

The study of CP violation in the  $B$  system is a standard benchmark process for  $b$  physics. The error in the CKM parameter  $\beta$  is  $\delta(\sin 2\beta) = (1+b)/D(1-2w)\sqrt{N(1+b)}$ , where the dilution factor,  $D$ , is defined as  $D = x_d(1+x_d^2)$ ,  $N$  is the number of tagged events,  $w$  is the fraction of wrong sign tags and  $b$  is the background to signal ratio. Values of  $D$  and  $w$  have been extracted from a number of studies.

We have considered three scenarios:

- Central tracking and central lepton triggering/tagging;
- Central tracking but with lepton triggering/tagging over the full  $|\eta|$  range;
- Tracking and triggering over the full  $|\eta|$  range.

In accessing the resolution in  $\sin(2\beta)$  the increased number of events reconstructed in the forward tracker must be balanced against the degraded mass resolution in the forward direction. Background levels are obtained by scaling from CDF's  $B$  results. Expected DØ muon acceptances and efficiencies were used<sup>[25]</sup> together with mass resolutions and reconstruction efficiencies for the upgraded tracking system given by the fast simulation

package. Table 4 shows the results for our combined simulations of the upgraded detector. Figure. 19 shows the expected mass resolution for  $B \rightarrow J/\psi K_S^0$ .

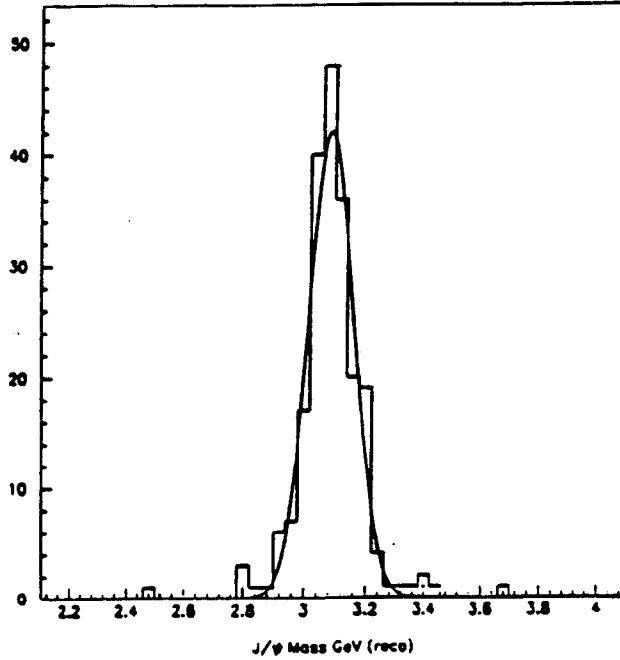


Figure 19. Mass resolution for  $B \rightarrow J/\psi K_S^0$  in the upgraded  $D\bar{0}$  detector, from the MCFAST simulation.

$B \rightarrow \psi K_s$	Central only	Central + full tag	Full $\eta$
Events in final state	430,000	430,000	430,000
Trigger	multi- $\ell$	multi- $\ell$	multi- $\ell$
Efficiency $\times$ Acceptance	0.0006	0.0011	0.0034
Tagged Events	236	492	1,443
Dilution factor	0.28	0.28	0.22
Error on $\sin(2\beta)$	0.24	0.16	0.12

Table 4. Precision obtained on  $\sin(2\beta)$  for  $1 fb^{-1}$  in the upgraded  $D\bar{0}$  detector, comparing the three scenarios listed.

It is clear that the CP violation measurement benefits substantially from lepton tagging and triggering ability over  $|\eta| \leq 3$ . While the advantage from covering this whole range for hadronic final state reconstruction is somewhat more modest due to the decreased

resolution at high  $|\eta|$ , it still yields a substantial improvement in the precision with which  $\sin(2\beta)$  can be measured.

### 3.5.4 Other $B$ -Physics Topics

Some of the other topics which we expect to focus on in our Run II  $B$ -Physics program are:

- Precision extraction of  $\alpha_S^2$  and  $\alpha_S^3$  processes;
- Study of  $B_c$  spectroscopy — the  $B_c$  system is a unique laboratory for heavy quark effective theories;
- Study of  $b$ -baryons;
- Searches for rare  $B$  decays such as  $B_d \rightarrow \pi/K \mu^+ \mu^-$  and  $B_d \rightarrow \mu^+ \mu^-$ .

## 3.6 Searches for New Phenomena

While the Standard Model is very successful in describing all the measurements of particle interactions currently available, it cannot be the whole story. It contains too many arbitrary parameters and the Higgs mechanism of electroweak symmetry breaking requires unnatural fine-tuning. Appealing theoretical frameworks which address these shortcomings have been suggested; examples include supersymmetry and new flavor symmetries. The spectrum of new states occurring in these models should be visible in the Tevatron Collider energy range. It is also necessary to search for completely unexpected new phenomena.

Searches for phenomena beyond the Standard Model have been an important part of DØ's physics menu to date. Their importance will continue to increase as greater accumulated luminosity stretches the reach into unexplored territory. The upgraded detector will maintain the unique DØ capabilities that have aided such searches in the past — the hermeticity of the calorimeter system, the excellent  $\cancel{E}_T$  resolution, and the large  $\eta$  coverage for lepton identification — and allow us to exploit the expanded capabilities of the detector to extend further into that territory.

### 3.6.1 An overview of new particle searches

Some of the searches we have already undertaken are summarized in Table 5. The top quark is included in the table as a cross section comparison. The production cross sections are rough estimates of the range accessible at the Tevatron's CM energy for Run Ia's luminosity. The table shows current DØ mass limits from Run Ia, for completed searches, and the estimated discovery reach for  $1fb^{-1}$ , for some of the searches. (The discovery reach is the mass which could be observed with a 10-event signal.)

Possible signals	Production cross sections (over accessible mass range)	Current Mass limit (model dependent)	Discovery reach 1 fb <sup>-1</sup>
$t\bar{t}$	$6.4 \pm 2.2$ pb	$199 \pm 30$ GeV (measured)	—
Right-handed $W$	0.5–1000 pb	540 GeV	
$W'$	$0.5-0.0001 \times \sigma_W$	600 GeV	$\sim 1$ TeV
$Z'$	$0.1-0.001 \times \sigma_Z$	480 GeV	$\sim 1$ TeV
scalar 1st generation leptoquarks	1.0–100 pb	130 GeV	$\sim 240$ GeV
scalar 2nd generation leptoquarks	1.0–100 pb	90 GeV	$\sim 240$ GeV
$\tilde{q}$ and $\tilde{g}$ pairs	5–1000 pb	140–200 GeV	$\sim 200-320$ GeV
gaugino pairs	0.5–10 pb	$< 47$ GeV	$\sim 90$ GeV
stop	0.1–100 pb	in progress	
$b'$	10–1000 pb	in progress	
$q^*$	0.1–100 pb	in progress	700 GeV

**Table 5.** Summary of  $D\bar{O}$ 's current limits and mass reach for the discovery of new particles (10 events required for discovery).

The table does not tell the complete story, however — while some exotic objects appear to be ruled out to quite large masses, this sometimes masks assumptions about branching ratios and/or coupling constants. There is still territory to be covered which requires triggering and analysis cuts to remain at fairly low  $E_T$  for the primary objects — jets, leptons, and  $\cancel{E}_T$  — and this should be an important consideration for the upgraded detector. Four examples of searches which will be advanced with the upgraded  $D\bar{O}$  detector are the  $Z'$  search, the gaugino search, the  $\tilde{t}$  search, and the  $\tilde{q} - \tilde{g}$  search, described below.

### 3.6.2 The $Z'$ search

The current mass limit on a heavy  $Z'$  from  $D\bar{O}$ 's search is 480 GeV, assuming the coupling of the  $Z'$  to leptons is identical to the Standard Model  $Z$ . The main determinant of the acceptance for this search is the  $\eta$  acceptance for lepton triggering and identification. The current  $D\bar{O}$  triggers for electrons reach out to  $\eta < 2.5$ . The discovery reach for  $Z'$  and  $W'$  in using electrons is shown as a function of integrated luminosity in Fig. 20. For the upgraded detector, these searches will benefit from an approximately

doubled acceptance through the use of muon as well as electron final states over all  $\eta \lesssim 3$ .

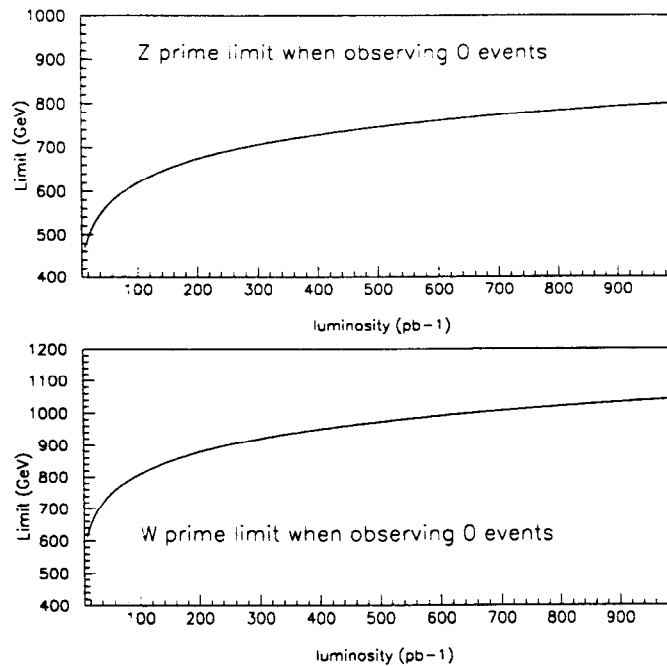


**Figure 20.** Mass reach for  $Z'$  and  $W'$  bosons over the luminosity range  $10 \text{ pb}^{-1} - 1 \text{ fb}^{-1}$ .

### 3.6.3 The gaugino search

Our current searches for supersymmetric gaugino pairs seek to probe the mass region from the LEP limit of approximately 47 GeV upward. While the production processes proceed through the electroweak interaction, the low mass still gives large enough cross sections to be explored with current data. The cleanest signature for  $\tilde{W}_1 - \tilde{Z}_2$  pair production is the 3 lepton +  $\cancel{E}_T$  topology. (The  $\cancel{E}_T$  comes from an escaping lightest supersymmetric particle, or LSP.) The highest  $E_T$  lepton in such events has a mean  $E_T$  of only 24 GeV for a  $\tilde{W}_1$  of mass 50 GeV, and the third lepton has a mean  $E_T$  of only 9 GeV. The upgraded detector is well-matched to this physics as it will operate with efficient (and unrescaled) electron and muon triggers for lepton transverse momenta down to  $p_T \sim 10 \text{ GeV}/c$ , and multilepton triggers may include muons as low as  $p_T \sim 1.5 \text{ GeV}/c$ . The gaugino search also requires full pseudorapidity coverage for lepton identification and measurement, as illustrated in Table 6 below which shows acceptance figures for a  $\tilde{W}_1$  with a mass of 50 GeV.

$\eta$ range	$eee$ (Leading $e$ )	$e\mu\mu$ ( $p_T^e > 5$ GeV)
0.0 - 1.0	58.3%	57.1%
1.4 - 2.5	21.0%	22.6%
2.5 - 3.4	2.2%	3.0%
	Any electron ( $p_T^e > 5$ GeV)	Any electron ( $p_T^e > 5$ GeV)
1.1 - 1.4	27.2%	13.2%
1.4 - 4.0	47.1%	26.3%

**Table 6.**  $D\bar{D}$  acceptance for 50 GeV  $\tilde{W}_1$ .

While the leading lepton is predominantly central, the acceptance for the three-lepton state is a factor of  $\sim 3$  larger for  $D\bar{D}$ 's full pseudorapidity coverage ( $|\eta| \lesssim 3$ ) than if lepton identification were restricted to  $|\eta| \lesssim 1$ .

### 3.6.4 The $\tilde{t}$ search

Within current SUSY theories, the large mass of the top quark carries the extremely interesting implication that its supersymmetric partner, the  $\tilde{t}$ , will be split into two mass eigenstates, one of which will be significantly less massive than the top quark itself. We have already carried out a search for this low mass  $\tilde{t}$  in the region where  $m_{\tilde{t}} < m_W + m_b$ , and will soon publish a limit contour in  $m_{\tilde{t}}$  vs.  $m_{LSP}$ . This is another search for which a relatively low mass region will remain interesting through Run II. The offline analysis for this search imposed a cut on  $\cancel{E}_T$  of 40 GeV, and a lower cut would have been desirable. We aim to maintain a trigger on pure  $\cancel{E}_T$ , or  $\cancel{E}_T + 1$  or 2 jets, with a threshold of  $\lesssim 50$  GeV and no prescale. While  $\cancel{E}_T$  trigger rates require some further study in the high luminosity regime, there appear to be no major problems. The reduced bunch spacing will mean that the number of interactions per crossing will be similar to that in Run Ib, and the faster calorimeter electronics will keep the pileup from out-of-time events in the calorimeter manageable. The upgraded inter-cryostat detector is also important for maintaining  $\cancel{E}_T$  precision. The search for the leptonic decay modes of the  $\tilde{t}$ , in the mass region heavier than the  $W$  but lighter than the top quark, will be very like the search for the top from 90 GeV to 200 GeV.

### 3.6.5 The $\tilde{q} - \tilde{g}$ search

The search for  $\tilde{q} - \tilde{g}$  pair production, like the  $\tilde{t}$  search, uses both leptonic and hadronic decay modes and relies heavily on the measurement of  $\cancel{E}_T$ . Our published limit<sup>[26]</sup> of 212 GeV for  $m_{\tilde{q}} = m_{\tilde{g}}$  is from the decay signature of multiple jets plus  $\cancel{E}_T$ , and the leptonic analysis is under way. In conjunction with the searches for  $\tilde{t}$  and gauginos, a combined analysis of these three SUSY signatures promises to make a significant contribution by either discovering SUSY or ruling out that portion of its (nearly infinite) parameter space most attractive to theorists.

It is important to stress that for the regime where the SUSY partners are in the range of 50-250 GeV, the Tevatron is the best place to make a SUSY discovery. The LHC detectors will have difficulty triggering at the low lepton  $E_T$ 's and  $\cancel{E}_T$  required to cover this range, in the presence of a large number of overlapping minimum bias events.

### 3.6.6 Other Searches

Many other searches for phenomena beyond the Standard Model have been and are being performed with the Run I data sets. Among these other searches are those for leptoquarks,  $b'$  quarks, excited quarks,  $W'$  bosons, right-handed  $W$ 's, heavy neutral leptons, charged Higgs, neutral Higgs, and massive stable particles. In addition, non-Standard Model behavior is being sought in distributions from known particles as well. Anomalous coupling analyses of  $W$  and  $Z$  data have produced limits, as will studies of QCD jet distributions. *All* of these searches will continue to be interesting in the upgrade era. Except for the QCD jet distribution studies, the acceptance, and therefore reach, of these searches depends on the ability to trigger on and identify leptons and  $\cancel{E}_T$ . Since limits on several interesting new particles will remain below 150 GeV into Run II, we have aimed to preserve our capacity to trigger as low as possible in  $E_T$  and  $\cancel{E}_T$ , and to make the  $\eta$  coverage for triggering and tracking as broad as possible.

## 3.7 Beyond Run II

Run II promises a rich and varied physics program at  $D\bar{D}$ . However, there remains much interesting high- $p_T$  physics which will require integrated luminosities an order of magnitude larger,  $\sim 10-30 \text{ fb}^{-1}$ . As an example, it has recently been suggested that it may be possible to observe light and intermediate mass Higgs bosons at the Tevatron collider, given sufficient integrated luminosity. Preliminary studies<sup>[27]</sup> indicate that the mass range  $80 \lesssim m_h \lesssim 130 \text{ GeV}$  may be accessible for integrated luminosities  $\mathcal{L} \gtrsim 10 \text{ fb}^{-1}$ . This mass range is of great interest, since minimal supersymmetric versions of the standard model almost always predict a light Higgs boson lying in this region. The possibility therefore exists of either discovering, or refuting, this whole class of models.

The channels of interest are  $(W/Z)h$  with  $W/Z \rightarrow$  leptons and  $h \rightarrow b\bar{b}$ , and  $W/Z \rightarrow$  jets and  $h \rightarrow \tau^+\tau^-$ . The reconstruction techniques needed for a Higgs discovery — jet-jet spectroscopy using  $b$ -tagging information — are similar to, and will benefit from, the high-statistics study of top quark production. In order to accumulate sufficient statistics, operation at luminosities higher than that currently envisaged for Run II would be desirable. We have made a preliminary study of triggering and data acquisition at  $\mathcal{L} = 2 \times 10^{33} \text{ cm}^{-2}\text{s}^{-1}$ <sup>[28]</sup>

and find no insuperable obstacles to triggering on and recording these Higgs final states. Of course, such physics is properly beyond the scope of the present Upgrade; it is mentioned in order to emphasize that high- $p_T$  physics at the Tevatron will remain of interest beyond Run II, and it is our belief that further luminosity increases are in fact desirable in order to fully exploit the physics opportunities. The upgraded detector described in this report provides a solid foundation for any additional enhancements that may be needed to meet the challenge of increased luminosity.

## 4. Conclusions

In this report we have described the upgrade to the DØ detector for Tevatron Run II, and outlined some of the physics which we intend to pursue. During this period, the Tevatron will be the highest energy accelerator available and will yield unsurpassed luminosity. We believe that the upgrade project satisfies the requirements of maintaining the excellent performance of the DØ detector while significantly improving its capabilities in the areas of  $b$ -tagging, and muon and electron identification and measurement. The result will be a versatile, general purpose detector, well-matched to the accelerator environment and to the physics requirements of Run II, with particular strengths complementary to those of CDF. We expect the upgraded DØ detector to play a leading role in carrying high energy physics into the twenty-first century.

## ACKNOWLEDGEMENTS

We thank the Fermilab Accelerator, Computing, and Research Divisions, and the support staffs at the collaborating institutions for their contributions to the success of this work. We also acknowledge the support of the U.S. Department of Energy, the U.S. National Science Foundation, the Commissariat à L'Energie Atomique in France, the Ministry for Atomic Energy and the Ministry of Science and Technology Policy in Russia, CNPq in Brazil, the Departments of Atomic Energy and Science and Education in India, Colciencias in Colombia, CONACyT in Mexico, the Ministry of Education, Research Foundation and KOSEF in Korea and the A.P. Sloan Foundation.

## REFERENCES

1. "The DØ Upgrade", unpublished (1990); "P823 (DØ Upgrade): Responses to the Physics Advisory Committee" DØ note 1148 (1991); "E823 (DØ Upgrade): R& D and Optimization Progress Report, DØ 1322 (1992); "E823 (DØ Upgrade): Step-1 and Beyond", DØ 1421 (1992); "E823 (DØ Upgrade): DØ $_{\beta}$ ", DØ 1733 (1993); "E823 (DØ Upgrade): Magnetic Tracking", DØ (1993).
2. D.D. Pitzl et al., Nucl. Phys. B (Proc. Suppl.) **23A** (1991) 340; H.J. Ziock et al., IEEE Trans. Nucl. Sci. **NS-38** (1991) 269.
3. "Tests of Silicon Microstrip Wedge Detectors for the DØ Experiment", C. Boswell, To appear in Proceedings of the 3<sup>rd</sup> International Workshop on Vertex Detectors, Bloomington, Indiana, May 8-13, 1994.
4. D. Adams et al., Fermilab-Conf-95/012E, January (1995).
5. M. Adams *et al.*, "A Detailed Study of Plastic Scintillating Strips with Axial Wavelength Shifting Fiber and VLPC Readout", to be submitted to Nucl. Inst. Meth. A.
6. S.A. Kleinfelder et al., Nucl. Phys. B (Proc. Suppl.), **23A**, 382 (1991).
7. Y. Arai, F. Sudo and T. Emura, KEK preprint 93-94, June 1993 H.
8. S. Abachi et al., (DØ Collaboration), Phys. Rev. Lett. **74** (1995) 2632.

9. E. Eichten and K. Lane, Phys. Lett. **327** (1994) 129.
10. C. Hill and S. Parke, Phys. Rev. **D49** (1994) 4454.
11. V. Barger and R.J.N. Phillips, MAD/PH/830 (1994).
12. K. Lane, BUHEP-95-2 (1995) and private communications.
13. Review of Particle Properties by the Particle Data Group, Phys. Rev. D50, No. 3, p.1173, August 1994.
14. J. Rosner, M.P. Worah, and T. Takeuchi, Phys. Rev. **D 49**, 1363 (1994).
15. F. Abe *et al.*, (CDF collaboration), Phys. Rev. Lett. **74** (1995) 341.
16. H.Weerts for the DØ collaboration, proceedings of the Tsukuba  $p \bar{p}$  conference, Tsukuba, Japan (1993).
17. S.Ellis, Z.Kunszt, and D. Soper, Phys. Rev. Lett. **62**, 2188 (1989); Phys. Rev. Lett. **64**, 2121 (1990).
18. W.Giele et al., "The Two-Jet Differential Cross Section at  $O(\alpha_s^3)$  in Hadron Collisions", Fermilab Pub-94/070-T. 1994.
19. G.Sterman, private communication.
20. W.Giele et al., Phys. Rev D46, 1980 (1992); Nucl.Phys. B403, 633 (1993).
21. H.Baer, J.Ohnemus, and J.Owens, Phys.Lett. **B234**, 127 (1990).
22. A.Brandenburg and O.Nachtmann, "Spin Effects and Factorization in Drell-Yan Process", Preprint HD-THEP-93-13, 1993.
23. S.Abachi et al., (DØ collaboration), Phys. Rev. Lett. **72** (1994) 2332.
24. MCFAST simulation package, Fermilab Computing Division.
25. D. Hedin and K. Johns, DØ note 2113 (1994).
26. S. Abachi et al., Fermilab PUB-95/057-E, submitted to Physical Review Letters.
27. A. Stange, W. Marciano and S. Willenbrock, Phys. Rev. **D50** (1994) 4491; S. Mrenna and G. Kane, UM-TH-94-24; A. Belyaev, E. Boos and L. Dudko, Mod. Phys. Lett. **A10** (1995) 25.
28. J. Womersley, DØ Note 2371 (1994).

\* Visitor from IHEP, Beijing, China.

‡ Visitor from CONICET, Argentina.

§ Visitor from Universidad de Buenos Aires, Argentina.

¶ Visitor from Univ. San Francisco de Quito, Ecuador.